

# CYCLO: Cyclic Graph Transformer Approach to Multi-Object Relationship Modeling in Aerial Videos

Trong-Thuan Nguyen<sup>1</sup>, Pha Nguyen<sup>1</sup>, Xin Li<sup>2</sup>, Jackson Cothren<sup>1</sup>,  
Alper Yilmaz<sup>3</sup>, Khoa Luu<sup>1</sup>

<sup>1</sup>University of Arkansas <sup>2</sup>State University of New York at Albany <sup>3</sup>Ohio State University

<sup>1</sup>{thuann, panguyen, khoa1uu, jcothre}@uark.edu <sup>2</sup>xli48@albany.edu <sup>3</sup>yilmaz.15@osu.edu

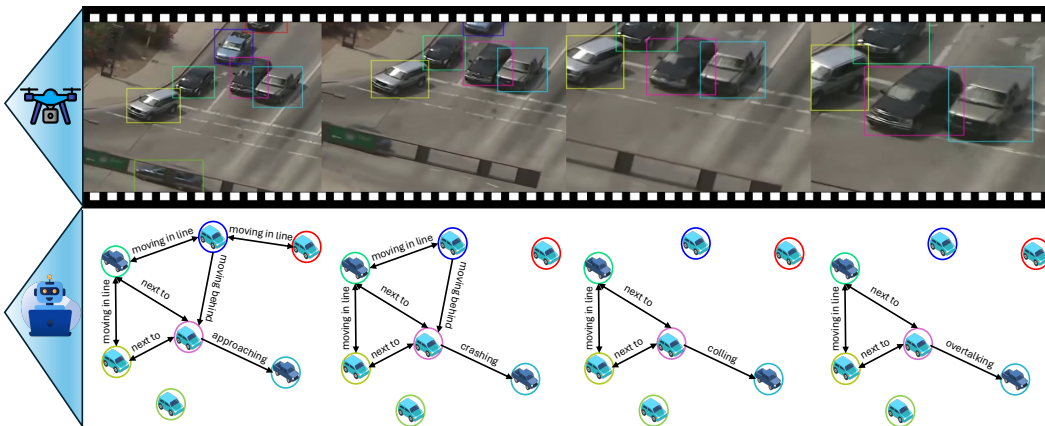


Figure 1: Multi-Object Relationship Modeling in Aerial videos analyzes a drone-captured video to detect and refine object relationships over time. The CYCLO model first identifies relationships between objects in individual frames and then incorporates temporal information about object positions and interactions to refine the understanding of those relationships across the video sequence. (Best viewed in colors)

## Abstract

Video scene graph generation (VidSGG) has emerged as a transformative approach to capturing and interpreting the intricate relationships among objects and their temporal dynamics in video sequences. In this paper, we introduce the new AeroEye dataset that focuses on multi-object relationship modeling in aerial videos. Our AeroEye dataset features various drone scenes and includes a visually comprehensive and precise collection of predicates that capture the intricate relationships and spatial arrangements among objects. To this end, we propose the novel Cyclic Graph Transformer (CYCLO) approach that allows the model to capture both direct and long-range temporal dependencies by continuously updating the history of interactions in a circular manner. The proposed approach also allows one to handle sequences with inherent cyclical patterns and process object relationships in the correct sequential order. Therefore, it can effectively capture periodic and overlapping relationships while minimizing information loss. The extensive experiments on the AeroEye dataset demonstrate the effectiveness of the proposed CYCLO model, demonstrating its potential to perform scene understanding on drone videos. Finally, the CYCLO method consistently achieves State-of-the-Art (SOTA) results on two in-the-wild scene graph generation benchmarks, *i.e.*, PVSG and ASPIRe.

# 1 Introduction

Visual scene understanding has shown significant progress in extracting semantic information from images and videos using deep learning algorithms [1, 2]. Building upon the significant progress in visual scene understanding using deep learning algorithms [1, 2], video scene graph generation (VidSGG) extends the concept of Scene Graph Generation (SGG) from static images to dynamic video, representing object relationships within a graph structure that evolves over time. VidSGG [3, 4, 5] focus on the temporal dimension by constructing a dynamic graph structure, encapsulating the spatial and temporal relationships among object interactions across frames. This helps in understanding human-object interactions [6, 7], temporal events [8, 9, 10], and reasoning [11, 12]. However, drone-captured videos present unique challenges due to larger image sizes and higher object density in Unmanned Aerial Vehicle (UAV) datasets [13, 14, 15]. Despite recent advances in tiny object detection [16, 17, 18], current algorithms still need to effectively model object interactions and their temporal evolution in aerial videos, which have various applications in surveillance, disaster response

In this paper, we introduce AeroEye, the first dataset for Video Scene Graph Generation in drone-captured videos featuring **Aerial-Oblique-Eye** views. AeroEye distinguishes itself by showcasing a rich tapestry of aerial videos and an extensive set of predicates describing the intricate relations and positions of multi-objects. To address multi-object relationship modeling in aerial videos from the AeroEye dataset, we propose the Cyclic Graph Transformer (CYCLO). This new approach can establish circular connectivity among frames and enables the model to capture direct and long-range temporal relationships. By continuously updating history across a ring topology, CYCLO allows the model to handle sequences with inherent cyclic patterns, facilitating the processing of object relationships in the correct temporal order. Furthermore, CYCLO provides several advantages to VidSGG, including the ability to model periodic and overlapping relationships, predict object interactions by reasoning from previous cycles, facilitate information transfer across frames, and efficiently utilize long sequences, addressing the limitations of previous methods [19, 5]. They usually struggle with long-term dependencies due to the diminishing influence of inputs over time.

**Contributions of this Work.** There are three main contributions to this work. First, we introduce a new *AeroEye* dataset for VidSGG in drone videos, augmented with numerous predicates and diverse scenes to capture the complex relationships in aerial videos. Second, we propose the CYCLO approach, utilizing circular connectivity among frames to enable periodic and overlapping relationships. It allows the model to capture long-range dependencies and process object interactions in the appropriate temporal arrangement. Finally, the proposed CYCLO approach outperforms prior methods on two large-scale in-the-wild VidSGG datasets, including PVSG [4] and ASPIRe [5]. Interestingly, using the same method (*e.g.*, our CYCLO), the ratio of correct predictions to incorrect predictions (R/mR) on AeroEye is higher than PVSG (Tables 4 and 6), despite having more predicates (Table A.11) and tiny objects. This suggests that our dataset is *less visually ambiguous* than PVSG.

## 2 Related Work

In this section, we first review the prior Visual Scene Graph Generation datasets and benchmarks. Then, we summarize the related Video Scene Graph Generation problems.

### 2.1 Visual Scene Graph Generation Datasets and Benchmarks

**Datasets.** VisDrone [14], DOTA [13], and SODA-A [23] image datasets, along with UAVid [33], UAVDT [24], and MAVREC [15] video datasets, offer high-resolution UAV datasets that enable precise object detection in dynamic scenes. While these UAV datasets focus on object detection, the Visual Genome [34] pioneered image-based SGG, and the Action Genome [3] dataset extended this concept to capture dynamic interactions within videos. Recently, ASPIRe [5] and SportsHHI [35] emphasize diverse human-object relationships and sports-specific player interactions. Additionally, PSG-4D [36] expands the VidSGG to encompass the 4D domain, bridging the gap between raw visual data and high-level understanding. In Table 1, we present a comparative overview of UAV-based and SGG datasets for images and videos, emphasizing their unique characteristics and advantages.

**Benchmarks.** The existing benchmark focuses on Image Scene Graph Generation (ImgSGG) and Video Scene Graph Generation (VidSGG). *ImgSGG* identifies and categorizes relationships between objects within an image into predefined relational categories, including Transformer-based

Table 1: Comparison of available datasets on drone images and videos. Viewpoints include drone-captured perspectives, which is our main focus in this work, including **aerial** (top-down), **oblique** (slanted), and **ground** (eye-level) perspectives. # denotes the number of corresponding items. The best values are **highlighted**. Full comparison with other scene graph generation benchmarks is in Table A.11

Datasets	#Videos	#Frames	Resolution	Annotations			#ObjCls	#RelCls	#Scenes	Viewpoints		
				BBox	Relation	#Instances				aerial	oblique	ground
DOTA [13]	-	11.3K	1490 × 957	✓	✗	2.2M	18	-	-	✓	✗	✗
AI-TOD [20]	-	28.1K	800 × 800	✓	✗	700.6K	8	-	-	✓	✗	✗
DIOR-R [21]	-	23.5K	800 × 800	✓	✗	192.5K	<b>20</b>	-	-	✓	✗	✗
MONET [22]	-	<b>53K</b>	-	✓	✗	162K	3	-	-	✓	✗	✗
SODA-A [23]	-	2.5K	<b>4761 × 2777</b>	✓	✗	<b>872.1K</b>	9	-	-	✓	✗	✓
VisDrone [14]	288	261.9K	3840 × 2160	✓	✗	<b>2.6M</b>	<b>10</b>	-	-	✓	✗	✗
UAVDT [24]	100	40.7K	1080 × 540	✓	✗	0.84M	3	-	6	✓	✗	✗
Stanford Drone [25]	<b>10K</b>	<b>929.5K</b>	-	✓	✗	-	6	-	8	✓	✗	✗
UTT-ADrone [26]	51	206.2K	1920 × 1080	✓	✗	210.5K	8	-	1	✓	✗	✗
ERA [27]	2.9K	343.7K	640 × 640	✓	✗	-	-	-	<b>25</b>	✓	✗	✗
MOR-UAV [28]	30	10.9K	1920 × 1080	✓	✗	89.8K	2	-	-	✓	✗	✗
AU-AIR [29]	-	32.8K	1920 × 1080	✓	✗	132K	8	-	-	✓	✗	✗
DroneSURF [30]	200	411.5K	1280 × 720	✓	✗	786K	1	-	-	✗	✓	✗
MiniDrone [31]	38	23.3K	224 × 224	✓	✗	-	-	-	1	✗	✓	✗
Brutal Running [32]	-	1K	227 × 227	✓	✗	-	-	-	1	✗	✓	✗
UAVid [33]	30	300	<b>4096 × 2160</b>	✓	✗	-	8	-	-	✗	✓	✗
MAVREC [15]	24	537K	3840 × 2160	✓	✗	1.1M	<b>10</b>	-	4	✗	✓	✓
AeroEye (Ours)*	<b>2.3K</b>	<b>261.5K</b>	<b>3840 × 2160</b>	✓	✓	<b>2.2M</b>	<b>56</b>	<b>384</b>	<b>29</b>	✓	✓	✓

\* CC-BY License of Creative Commons

methods [37, 38, 39, 40] and generative-based models [41, 42, 43]. *VidSGG* leverages the dynamic nature of object interactions over time to better identify relationships, as the temporal dimension of videos provides a richer context for understanding semantic connections within the scene. Current methods using hierarchical structures [44, 5] or Transformer architectures [19, 45, 46] excel at capturing long-range dependencies and complex interactions, advancing video understanding in video captioning [8, 9, 10], visual question answering [11, 12], and video grounding [47, 48, 49].

## 2.2 Video Scene Graph Generation

VidSGG can be categorized into two main types based on the granularity of its graph representation. *Video-level SGG* represents object trajectories as graph nodes, capturing constant relations between objects for a video. Various methods have been proposed to address this problem, incorporating Conditional Random Fields [50], abstracting videos [51], and iterative relation inference techniques [52] on fully connected spatio-temporal. However, focusing primarily on recognizing video-level relations directly based on object-tracking results and neglecting frame-level scene graphs results in a cumbersome pipeline highly dependent on tracking accuracy. In contrast, *Frame-level SGG* defines the graph at the frame level, allowing relations to change over time. The releases of the benchmark datasets [53, 4, 5] have prompted the development of VidSGG models. TRACE [44], for instance, employs a hierarchical relation tree to capture spatio-temporal context information, while CSTTran [19] uses a spatio-temporal transformer to solve the problem. Recently, hierarchical interlacement graph (HIG) [5] abstracts relationship evolution using a sequence of hierarchical graphs.

## 2.3 Discussions

In this subsection, we conceptually compare our proposed approach with relationship modeling concepts discussed in Section 2.2 as illustrated in Fig. 2. In addition, we highlight the advantages of our approach and discuss the properties that distinguish it from these existing methods.

**Concepts.** The *progressive* approach fuses pairwise features between object pairs at each frame, encoding the object relationship at that specific step, followed by a fully connected layer to classify the predicate types. However, it processes frames independently without considering the temporal context. The *batch-progressive* approach employs a transformer block with positional embeddings on the fused query features. The *hierarchical* approach represents a video as a sequence of graphs, integrating temporal and spatial information at different levels. The node and edge features are updated at each hierarchical level based on the previous level to capture evolving object relationships.

**Limitations.** While the *batch-progressive* approach considers temporal information, both these *progressive* and *batch-progressive* approaches have limitations in modeling the full complexity of temporal dynamics and dependencies in the video. In contrast, the *hierarchical* graph approach can

capture complex interactions and relationships between objects by considering the temporal evolution of graphs at different granularity levels. However, the hierarchical graph requires observation of the entire video to construct the graph (*i.e.*, offline method).

**Advantages of Our Design.** Inspired by previous work [54, 55], which processes temporal features through iterative feedback loops and circular updating, we propose the CYCLO approach that circularly incorporates an updated history of relationships. In contrast to these methods, which focus on frame-level updates influenced by global features, our approach constructs and refines scene graphs for each frame, capturing static spatial relationships between objects and their dynamic evolution over time. By leveraging circular connectivity, CYCLO establishes a continuous loop of temporal information, ensuring no temporal edge is treated as a boundary. It enables the Transformer to operate online and then capture and update relationships between objects more effectively, correcting erroneous connections. The theoretical properties are included in Section B of Appendices.

### 3 The Proposed AeroEye Dataset

In this section, we detail the AeroEye dataset annotation process and provide the dataset statistics.

#### 3.1 Dataset Collection

**Data Preparation.** We leverage videos from the ERA [27] and MAVREC [15] datasets to construct our AeroEye dataset. ERA consists of diverse scenes ranging from rural to urban environments in extreme conditions (*e.g.* earthquake, flood, fire, mudslide), daily activities (*e.g.* harvesting, plowing, party, traffic collision), and sports activities (*e.g.* soccer, basketball, baseball, running, swimming). MAVREC features sparse and dense object distributions and contains typical outdoor activities characterized by many vehicle classes, incorporating viewpoint changes and varying illumination.

**Relationship Classes and Instance Formulation.** In Fig. 3, we focus on two aspects of object relationships: positions (*e.g.* in front of, behind, next to) and relations, which consist of movement actions (*e.g.* chasing, towing, overtaking) and collision actions (*e.g.* hitting, crashing, colliding). These relationships are semantically complex and require detailed spatio-temporal context reasoning for recognition. Following previous datasets [3, 4, 5], we define relationship instances at the frame level, considering the long-term spatial-temporal context. Each instance is formulated as a triplet  $\langle s, o, p \rangle$ , where  $s$  and  $o$  denote the bounding boxes of the subject and object, and  $p$  represents the predicate, included in Table A.8 and Table A.9 and summarized in Fig. 4.



Figure 4: Relationship word cloud on AeroEye dataset.

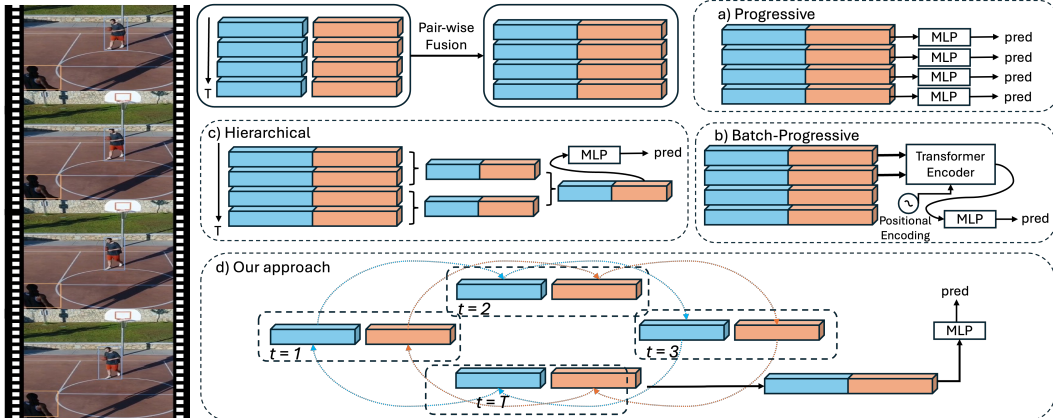
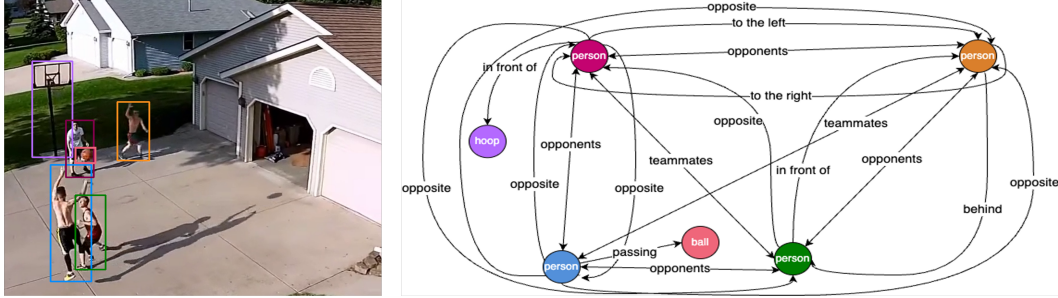


Figure 2: Comparisons of CYCLO and existing relationship modeling: (a) *Progression* [37, 52]: frame-wise fusion and classification; (b) *Batch-progression* [19, 45, 46]: temporal transformer; (c) *Hierarchy* [5]: spatiotemporal graph; (d) Our CYCLO approach: circular connectivity for capturing temporal dependencies.





a) Basketball scene from the ERA dataset      b) A scene graph depicting our annotations of relationships between objects.

Figure 3: Example annotation in our dataset. In Fig. 3b, straight arrows denote relationships between objects, while curved arrows indicate the positions of the objects. Nodes of the same color represent the same object, and the labels on the edges specify the predicate of each relationship. (Best viewed in colors)

### 3.2 Data Specification

**Data Annotation.** We annotate keyframes at 5FPS to capture frequent and rapid changes in positions and relations in aerial videos, reducing redundancy while keeping up with interaction changes. Our two-stage annotation pipeline first performs *object localization and tracking* and then *relationship instance annotation*. Although we annotate relationship instances frame by frame illustrated in Fig. 3, we easily create relationship tubes using the provided object tracking ID by connecting the same pair of objects with the same relationship predicate across consecutive frames. The annotation file includes object information (*i.e.*, bounding boxes, category names, and tracking IDs) and relationships within each frame. The quality control and annotation examples are discussed in Section A.2 of Appendices.

**Data Statistics.** The AeroEye dataset is a collection of 2,260 videos with 261,503 frames, annotated with over 2.2 million bounding boxes across 56 object categories typically observed from *aerial*, *oblique*, and *ground* perspectives captured by drone. Specifically, our AeroEye dataset consists of 384 predicates divided into two relationship categories: 135 positions and 249 relations. The key strength of AeroEye is its richness in relationships. On average, each video in the dataset has 127 frames, providing moderate temporal depth for capturing detailed interactions. The average number of frames per scene is 8,970, indicating substantial variability and complexity. AeroEye is rich in relationships, with more than 43 million relationship instances. In Table 1, we provide a detailed comparison with related datasets, while Fig. 5 presents statistics on the AeroEye dataset. In addition, predicate definitions and additional statistics are discussed in Sections A.1 and A.4 of the Appendices.

## 4 The Proposed Approach

In this section, we introduce the CYCLO approach, which consists of two main components, including the Spatial Attention Graph and the Cyclic Temporal Graph Transformer.

### 4.1 Problem Formulation

Given an input video with  $T$  frames, we construct dynamic scene graphs  $\{\mathcal{G}_t\}_{t=1}^T$  that encode the relationships among objects within these frames. Each graph  $\mathcal{G}_t(\mathcal{V}_t, \mathcal{E}_t)$  captures static relationships,

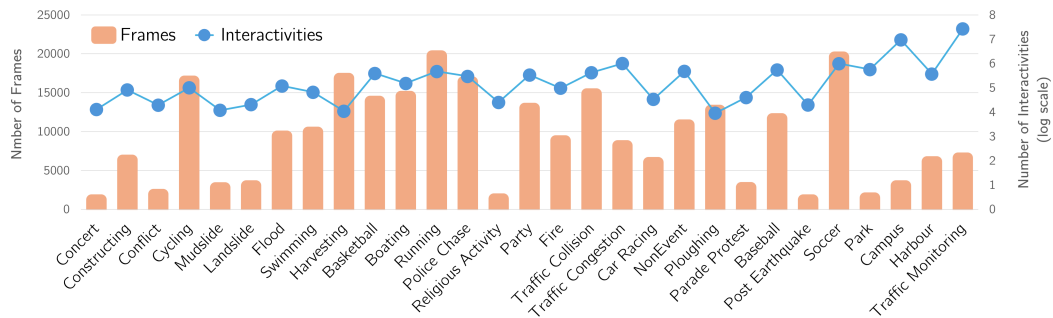


Figure 5: Statistics for each scene on the AeroEye dataset.

where node  $\mathcal{V}$  consists of objects and edge  $\mathcal{E}$  denotes the relationship between objects. Each object  $v_i \in \mathcal{V}$  has an object category  $v_i^c \in \mathcal{C}_v$  and box coordinates  $v_i^b \in [0, 1]^4$ . Each relationship  $e_j \in \mathcal{E}$  represents the  $j$ -th triplet  $(s_j, o_j, p_j)$ , where subject  $s_j$  and object  $o_j$  and predicate  $p_j \in \mathcal{C}_p$ .

## 4.2 Spatial Attention Graph

Self-attention mechanisms in one-stage object detectors [56, 16] model relationships between objects, allowing insights into the dynamics between entities without relying on additional contextual information. For example, in an aerial parking lot video with cars, vans, and people, if the self-attention layer strongly connects the queries representing the person and the car, it suggests an interaction, such as the person entering the vehicle. Inspired by [40], in our CYCLO approach, to construct the static graph in each frame  $t$ , we utilize the DETR decoder to establish bidirectional connections among object queries. In particular, we compute relational representations at each layer  $l$  by concatenating the query and key vectors,  $Q_t^l$  and  $K_t^l$ , for every object pair. This process ensures the layer  $l - 1$  output seamlessly transitions as input to layer  $l$ . We omit the superscript  $L$  related to the final layer to simplify the following discussion. At each frame,  $\widehat{R}_{a,t}^l$  captures the dynamic interplay of relations at layer  $l$ , utilizing their query and key vectors. Furthermore,  $\widehat{R}_{z,t}$  leverages object queries in the final layer for object detection. These relationships are formally defined as in Eqn. (1).

$$\widehat{R}_{a,t}^l = [Q_t^l \phi_{W_s^l}; K_t^l \phi_{W_o^l}], \quad \widehat{R}_{z,t} = [\widehat{Z}_t \phi_{W_s}; \widehat{Z}_t \phi_{W_o}] \quad (1)$$

Here,  $\phi_{W_s}$  and  $\phi_{W_o}$  are the linear transformations that process subject and object features, enabling the model to consider both object characteristics and their interrelationships comprehensively. In addition, gating mechanisms  $g_{a,t}^l$  and  $g_{z,t}$  dynamically modulate the contributions from different layers. These gated representations from all layers are then integrated to construct a relation matrix:

$$\begin{aligned} \widehat{g}_{a,t}^l &= \sigma(\widehat{R}_{a,t}^l \phi_{W_G}), \quad \widehat{g}_{z,t} = \sigma(\widehat{R}_{z,t} \phi_{W_G}) \\ \widehat{R}_t &= \sum_{l=1}^L (\widehat{g}_{a,t}^l \times \widehat{R}_{a,t}^l) + \widehat{g}_{z,t} \times \widehat{R}_{z,t} \end{aligned} \quad (2)$$

where  $\phi_{W_G}$  denotes the linear weight applied during the gating process. Finally, the relation matrix is fed into the three-layer perception (MLP) with ReLU activation and a sigmoid function  $\sigma$ , which predicts multiple relationships ( $p_j$ ) between pairs of objects ( $s_j, o_j$ ). Mathematically,  $\widehat{G}_t = \sigma(\text{MLP}(\widehat{R}_t))$  is the graph representation at frame  $t$ -th, where  $\widehat{G}_t \in \mathbb{R}^{N \times N \times |\mathcal{C}_p|}$ .

**Discussion.** Transformer-based approaches to VidSGG effectively capture interactions and temporal changes through self-attention mechanisms, creating detailed scene graphs that reflect video dynamic relationships. However, these models often struggle to represent the directional and historical aspects of the relationship accurately. While effective at identifying token correlations, the scaled dot-product fails to consider their temporal or spatial ordering. This oversight is particularly critical in videos, where understanding the historical context of relationships is essential. For example, the sequence of relationships leading up to a car crash, including speeding, lane changing, and passing, must be considered. Each interaction change provides crucial historical information that contextualizes the final relationships, vital for enhancing prediction and interpretation. In addition, traditional self-attention [57] does not adequately capture this essential sequential, *directional*, and *historical information* [58]. It highlights the need for advancements in transformer architectures to more effectively integrate the direction and historical sequence of interactions within videos.

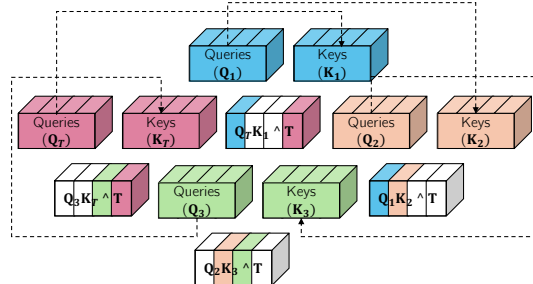


Figure 6: Illustration of cyclic interactions in the Cyclic Spatial-Temporal Graph Transformer. Each frame, represented by a colored block (where the first frame,  $t = 1$  and the last frame,  $T = 4$ ), undergoes spatial attention to obtain queries ( $Q_t$ ) and keys ( $K_t$ ).

## 4.3 Cyclic Temporal Graph Transformer

We present the Cyclic Spatial-Temporal Graph Transformer to refine the spatial attention graph in each scene, capturing temporal dependencies via subject-object relationships across adjacent frames.

**Cyclic Attention.** As mentioned in Section 4.2, self-attention does not adequately capture *directional* and *historical information*. Therefore, we propose the cyclic attention (CA), defined as in Eqn. (3).

$$\text{CA}(Q_t, K_t) = \sum_{i=0}^{T-1} \sigma \left( \frac{Q_t (K_{\eta(t+i) \bmod T})^\top}{\sqrt{d_{\text{head}}}} \right) \quad (3)$$

In Eqn. (3),  $\eta$  is a shift term enabling **cyclical indexing** via  $(\bmod T)$ . This cyclical indexing, illustrated in Fig. 6, allows for continuous sequence processing by connecting the end to the beginning, which is crucial for predicting movements in dynamic interactions where past events influence future actions (e.g. a car navigating a roundabout). Different from the standard self-attention (Eqn. (B.21)), which is permutation equivariant without positional encodings, the cyclical indexing in cyclic attention that is *non-permutation equivariant*. This property is crucial for multi-object relationship modeling as discussed in Subsection 4.2. Detailed explanations are included in Section B.4 of the Appendices.

**Temporal Graph Transformer.** Our Temporal Graph Transformer refines spatial attention graphs,  $\{\widehat{G}_t\}_{t=1}^T$ , into a sequence of dynamic graphs,  $\{G_t\}_{t=1}^T$ , leveraging the temporal dynamics and spatial interactions of objects across video frames. Our approach employs a series of cyclic attention blocks configured within multi-head attention to refine object representations by integrating features from adjacent frames. The core of our approach is the integration of cyclic attention into a multi-head structure, which processes the sequence of input features  $\widehat{Z} = \{\widehat{Z}_t\}_{t=1}^T$ , represented as in Eqn. (4).

$$\begin{aligned} Z' &= \phi_{W_c}([h_0; h_1; \dots; h_{e-1}]), & Z'_t &= \phi_{W_c}([h_0(t); h_1(t); \dots; h_{e-1}(t)]), \\ h_i(t) &= \text{CA}(\phi_{W_q^i}(\widehat{Z}_t), \phi_{W_k^i}(\widehat{Z})), & i &\in \{0, 1, \dots, e-1\}, \end{aligned} \quad (4)$$

where  $\phi_{W_c}$ ,  $\phi_{W_q^i}$ , and  $\phi_{W_k^i}$  denote the linear transformations. Each head  $h_i(t)$  computes the cyclic attention, integrating information across the video to enhance the temporal relationship at each frame. The outputs from various heads at each frame are integrated into  $Z'_t$ , derived from concatenating all attention head outputs. These heads process features cyclically across different representation subspaces to capture the temporal evolution of relationships in the video. Then,  $Z$  is obtained by applying layer normalization (LN) and a skip connection to the aggregated features  $Z'_t$ , where  $Z = \text{LN}(Z' + \widehat{Z})$ . This step ensures that  $Z'_t$  is stabilized and effectively integrated with the original features  $\widehat{Z}$ , thus dynamically updating the scene graph and ensuring temporal coherence.

In addition,  $Z_t$  is utilized to construct a new relation matrix  $R_t$  by applying the transformations in Eqn. (1) and (2). This updated matrix  $R_t$  refines the relationship dynamics captured in static frames by correcting spurious or incomplete relationships and incorporating previously omitted ones using the temporal context from the frame sequence. As a result,  $G_t$  comprehensively represents persistent and transient interactions, including their direction and historical sequence within the video.

**Loss Function.** Visual object relationships often involve similar predicates (e.g. parking next to and stopping next to). Thereby, we use multi-label margin loss, as in [19]:

$$\mathcal{L}_p(r, \mathcal{P}^+, \mathcal{P}^-) = \sum_{p \in \mathcal{P}^+} \sum_{q \in \mathcal{P}^-} \max(0, 1 - \phi(r, p) + \phi(r, q)) \quad (5)$$

Here,  $r$  is a subject-object pair, with  $\mathcal{P}^+$  and  $\mathcal{P}^-$  representing positive and negative predicates, respectively. Additionally, object distributions are determined using neural networks with ReLU and batch normalization, applying cross-entropy loss. The total loss combines these two losses.

## 5 Experimental Results

In this section, we discuss the benchmark dataset evaluations and comparisons with SOTA methods.

### 5.1 Implementation Details

**Dataset.** We use 10-fold cross-validation on the AeroEye dataset, including 1,797 videos for training and 463 videos for testing. We also evaluate our performance on PVSG [4] and ASPIRe [5] datasets.

**Settings.** We employ DINO [16] to extract the spatial attention graphs (in Section 4.2). DINO is trained with ResNet-50 backbone and 1500 queries on MAVREC, achieving 92.35 mAP on the validation set. The pre-trained detector is applied to baselines, and parameters are fixed during

Table 2: Our performance (%) on AeroEye for varying shift terms at Recall (R) and mean Recall (mR).

Shift Value	PredCls			SGCls			SGDet		
	R/mR@20	R/mR@50	R/mR@100	R/mR@20	R/mR@50	R/mR@100	R/mR@20	R/mR@50	R/mR@100
1	<b>56.20 / 19.23</b>	<b>61.62 / 20.67</b>	<b>62.40 / 21.19</b>	<b>54.15 / 16.22</b>	<b>59.59 / 18.20</b>	<b>60.37 / 18.38</b>	<b>43.53 / 13.29</b>	<b>47.93 / 13.69</b>	<b>48.94 / 13.86</b>
2	55.01 / 18.01	60.02 / 19.02	61.03 / 19.53	53.04 / 15.05	58.06 / 17.07	59.08 / 17.25	42.09 / 12.10	46.11 / 12.56	47.12 / 12.78
3	54.12 / 17.11	59.13 / 18.12	60.14 / 18.63	52.17 / 14.18	57.19 / 16.20	58.21 / 16.42	41.28 / 11.30	45.30 / 11.82	46.32 / 12.04
4	54.55 / 17.55	59.56 / 18.56	60.57 / 19.07	52.59 / 14.60	57.61 / 16.62	58.63 / 16.84	41.75 / 11.76	45.77 / 12.28	46.79 / 12.50
5	54.33 / 17.34	59.35 / 18.36	60.37 / 18.88	52.40 / 14.41	57.42 / 16.43	58.44 / 16.65	41.50 / 11.51	45.53 / 12.03	46.55 / 12.26

Table 3: Our performance (%) on AeroEye for varying frames per video at Recall (R) and mean Recall (mR).

# Frame Discarded	PredCls			SGCls			SGDet		
	R/mR@20	R/mR@50	R/mR@100	R/mR@20	R/mR@50	R/mR@100	R/mR@20	R/mR@50	R/mR@100
1	<b>56.20 / 19.23</b>	<b>61.62 / 20.67</b>	<b>62.40 / 21.19</b>	<b>54.15 / 16.22</b>	<b>59.59 / 18.20</b>	<b>60.37 / 18.38</b>	<b>43.53 / 13.29</b>	<b>47.93 / 13.69</b>	<b>48.94 / 13.86</b>
2	55.08 / 18.82	60.39 / 20.26	61.15 / 20.76	53.07 / 15.90	58.40 / 17.84	59.16 / 18.01	42.66 / 13.02	46.97 / 13.41	47.96 / 13.58
3	53.98 / 18.42	59.18 / 19.85	59.93 / 20.34	51.99 / 15.58	57.23 / 17.49	57.97 / 17.65	41.81 / 12.75	46.03 / 13.14	47.00 / 13.30
4	52.90 / 18.04	57.99 / 19.46	58.73 / 19.93	50.95 / 15.27	56.08 / 17.14	56.81 / 17.30	40.97 / 12.49	45.11 / 12.87	46.06 / 13.03
5	51.84 / 17.66	56.83 / 19.08	57.55 / 19.53	49.93 / 14.96	54.96 / 16.80	55.68 / 16.96	40.17 / 12.24	44.23 / 12.61	45.14 / 12.76

Table 4: Comparison (mean  $\pm$  std) on AeroEye against baseline methods in terms of Recall (R).

Method	PredCls			SGCls			SGDet		
	R@20	R@50	R@100	R@20	R@50	R@100	R@20	R@50	R@100
Vanila (2a)	50.12 $\pm$ 1.80	54.68 $\pm$ 5.70	56.32 $\pm$ 3.45	48.09 $\pm$ 1.78	53.23 $\pm$ 5.66	54.99 $\pm$ 3.38	31.04 $\pm$ 3.41	34.28 $\pm$ 0.72	34.62 $\pm$ 1.10
Transformer (2b)	53.25 $\pm$ 1.71	59.35 $\pm$ 4.02	60.89 $\pm$ 0.88	51.12 $\pm$ 1.66	57.12 $\pm$ 3.91	59.19 $\pm$ 0.83	41.09 $\pm$ 0.42	46.52 $\pm$ 0.63	47.15 $\pm$ 0.83
HIG (2c)	54.18 $\pm$ 1.23	59.59 $\pm$ 5.90	60.35 $\pm$ 5.30	52.03 $\pm$ 1.19	57.47 $\pm$ 5.87	58.18 $\pm$ 5.22	37.28 $\pm$ 0.60	38.59 $\pm$ 2.37	39.27 $\pm$ 1.49
CYCLO (2d - Ours)	<b>56.20 <math>\pm</math> 0.70</b>	<b>61.62 <math>\pm</math> 2.90</b>	<b>62.40 <math>\pm</math> 1.88</b>	<b>54.15 <math>\pm</math> 0.67</b>	<b>59.59 <math>\pm</math> 2.82</b>	<b>60.37 <math>\pm</math> 1.83</b>	<b>43.53 <math>\pm</math> 0.30</b>	<b>47.93 <math>\pm</math> 0.65</b>	<b>48.94 <math>\pm</math> 0.79</b>

subsequent task training. Our model is trained on  $8 \times$  A600 GPUs using 12 epochs with AdamW optimizer (initial learning rate of  $1e^{-5}$  and a batch size of 1), gradient clipping (max norm of 5).

**Evaluation Metrics.** We evaluate models on two standard tasks in image-based scene graph generation followed by previous work [59, 4] that are predicate classification (*PredCls*), scene graph classification (*SGCls*), and scene graph detection (*SGDet*). While *SGCls* predicts relationships given ground truth objects, *SGDet* involves detecting objects and predicting relationships. These tasks are evaluated using Recall (R@K) and mean Recall (mR@K), where  $K \in \{10, 20, 50\}$ .

## 5.2 Ablation Study

**Semantic Dynamics in Cyclic Attention.** By altering  $\eta$  (in Eqn. (3)), we consider the permutation or non-equivariance equivariance. If the predictions systematically adapt to the shifts induced by different  $\eta$  values, it demonstrates a degree of *permutation equivariance*. Conversely, if the predictions change in ways that do not correspond systematically to these shifts, it may indicate *non-permutation equivariance*. Table 2 shows a decrease performance, implying disrupted temporal patterns and *non-permutation invariance*, indicated by unpredictable output changes relative to input shifts.

**Cyclic Dependency.** To further validate the *cyclic* dependency of our model, we discarded frames from every successive frame. Removing frames disrupts the temporal continuity of the sequence, which is crucial for maintaining the the cyclic nature of video. If the cyclic model presupposes that each frame has direct relationships with its adjacent frames circularly, then removing frames could sever these relationships, potentially diminishing the ability to leverage cyclical patterns effectively. Indeed, Table 3 reveals a decrease at Recall and mean Recall when frames were reduced.

## 5.3 Comparisons with Baseline Methods

Table 4 shows CYCLO outperforms other methods (Section B.3) across metrics and tasks, surpassing Transformer by 2.95%, 3.03%, and 2.44% in the *PredCls*, *SGCls*, and *SGDet* at R@20, and maintaining its lead even at higher Recall thresholds. Moreover, Table 5 shows significant improvements at mR@20, mR@50, and mR@100, with CYCLO leading HIG by 0.86% in the *PredCls* task at mR@20 and exceeding HIG by 1.12% and 1.32% in the *SGCls* and *SGDet* tasks, respectively, at mR@20. In addition, the consistent performance and low standard deviation of the CYCLO model across Table 4 and 5 demonstrate its robustness and overall superiority. Fig. 7 displays that CYCLO can capture the evolving relationships between objects by updating their positions and interactions.

## 5.4 Comparisons with State-of-the-Art Methods

Table 5: Comparison (mean  $\pm$  std) on AeroEye against baseline methods in terms of mean Recall (mR).

Method	PredCls			SGCls			SGDet		
	mR@20	mR@50	mR@100	mR@20	mR@50	mR@100	mR@20	mR@50	mR@100
Vanila (2a)	12.21 $\pm$ 0.51	13.34 $\pm$ 0.62	13.58 $\pm$ 0.73	8.05 $\pm$ 0.42	8.15 $\pm$ 2.65	8.77 $\pm$ 1.63	11.20 $\pm$ 2.38	11.27 $\pm$ 0.84	12.43 $\pm$ 0.68
Transformer (2b)	14.25 $\pm$ 0.46	15.78 $\pm$ 0.53	16.24 $\pm$ 0.58	11.12 $\pm$ 0.35	13.12 $\pm$ 1.53	13.69 $\pm$ 1.32	11.88 $\pm$ 0.05	12.31 $\pm$ 0.13	12.91 $\pm$ 0.15
HIG (2c)	18.37 $\pm$ 0.68	19.85 $\pm$ 0.79	20.43 $\pm$ 0.88	15.10 $\pm$ 0.37	17.08 $\pm$ 2.66	17.69 $\pm$ 1.79	11.97 $\pm$ 1.07	13.12 $\pm$ 2.43	13.29 $\pm$ 2.41
CYCLO (2d - Ours)	<b>19.23 <math>\pm</math> 0.32</b>	<b>20.67 <math>\pm</math> 0.42</b>	<b>21.19 <math>\pm</math> 0.48</b>	<b>16.22 <math>\pm</math> 0.04</b>	<b>18.20 <math>\pm</math> 1.29</b>	<b>18.38 <math>\pm</math> 0.43</b>	<b>13.29 <math>\pm</math> 0.46</b>	<b>13.69 <math>\pm</math> 0.53</b>	<b>13.86 <math>\pm</math> 0.55</b>

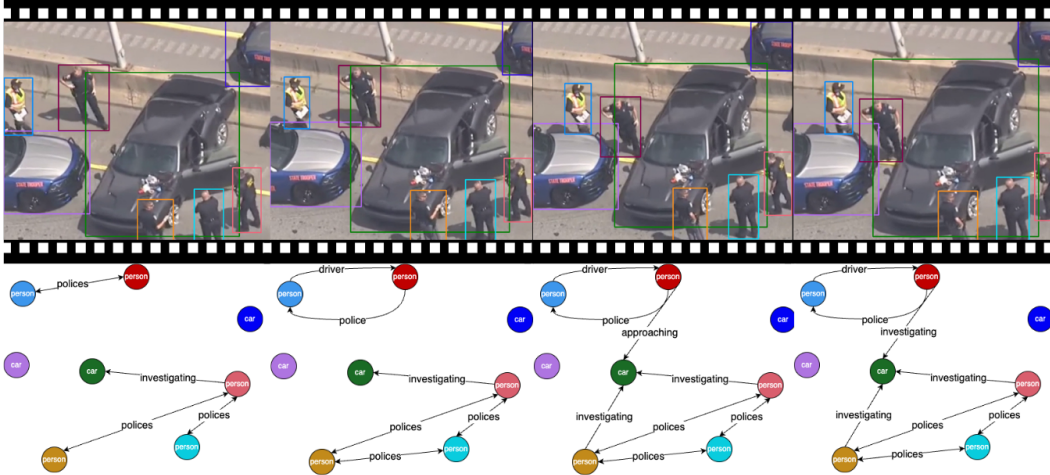


Figure 7: Scene graphs generated by the CYCLO model on the AeroEye dataset. (Best viewed in colors)

**Performance on PVSG.** Table 6 shows that the CYCLO model outperforms other models on the PVSG dataset, achieving the highest Recall and mean Recall. CYCLO surpasses HIG and Transformer by 1.23% and 1.81% at R@20, respectively, and outperforms them in R@50 and R@100. CYCLO also slightly improves mean Recall, demonstrating its robustness in periodic actions in PVSG (*e.g.*, cooking, washing).

**Performance on ASPIRe.** The ASPIRe dataset comprises five interactivity types; however, we focus on position and relation for a fair comparison. Table 7 shows that CYCLO consistently outperforms existing methods across varying recall and mean recall thresholds. Regarding R@20, our model higher 0.69% and 5.03% than HIG for position and relation. Moreover, CYCLO significantly improves the mean Recall at every threshold, revealing that our proposed approach can address the long-tail distribution of the ASPIRe dataset.

## 6 Conclusions

We have presented CYCLO, an approach that captures periodic and overlapping relationships, handles long sequences, and minimizes information loss. We also introduced AeroEye, a diverse dataset of drone-captured scenes with complex object relations and positions. Extensive experiments on AeroEye, ASPIRe, and PVSG datasets demonstrate the effectiveness of our approach.

**Limitations.** Although CYCLO has achieved impressive performance, it may reveal limitations when dealing with incomplete or discontinuous videos. The periodic and cyclic attention mechanisms, crucial for capturing temporal and spatial object relationships, heavily rely on video continuity and completeness. Interruptions in the sequence, such as missing or discontinuous frames, disrupt the formation of accurate cyclical references, leading to inconsistent and incorrect predictions.

**Broader Impacts.** The proposed approach advances VidSGG which enables better capture of object interactions and temporal evolution in aerial videos, which is crucial for surveillance, disaster response, traffic management, and precision agriculture applications. However, it is important to consider the potential misuse of the proposed approach, such as unauthorized surveillance.

Table 6: Comparative performance (%) of our model and previous methods on the PVSG dataset, evaluated by Recall (R) and mean Recall (mR).

Model	R/mR@20	R/mR@50	R/mR@100
Vanilla (2a)	2.35 / 1.22	2.71 / 1.31	2.94 / 1.45
Handcrafted (2b)	2.56 / 1.24	2.78 / 1.35	3.05 / 1.54
1D Convolution (2b)	2.79 / 1.24	2.80 / 1.47	3.10 / 1.59
Transformer (2b)	4.02 / 1.75	4.41 / 1.86	4.88 / 2.03
HIG (2c)	4.60 / 1.89	4.88 / 2.05	5.43 / 2.23
<b>CYCLO (2d - Ours)</b>	<b>5.83 / 1.98</b>	<b>6.12 / 2.15</b>	<b>6.70 / 2.34</b>

Table 7: Comparative performance (%) of our model and previous methods on the ASPIRe dataset.

Model	Interactivity	R/mR@20	R/mR@50	R/mR@100
Vanilla (2a)	Position	10.52 / 0.50	21.97 / 0.55	38.05 / 0.62
	Relation	9.71 / 0.32	21.96 / 0.36	39.11 / 0.40
Handcrafted (2b)	Position	10.73 / 0.52	22.04 / 0.59	38.16 / 0.71
	Relation	9.92 / 0.34	22.03 / 0.40	39.22 / 0.49
1D Convolution (2b)	Position	10.96 / 0.52	22.06 / 0.71	38.21 / 0.76
	Relation	10.15 / 0.34	22.05 / 0.52	39.27 / 0.54
Transformer (2b)	Position	11.04 / 0.83	22.52 / 0.90	38.84 / 1.02
	Relation	10.23 / 0.65	22.51 / 0.71	39.90 / 0.96
HIG (2c)	Position	13.02 / 0.09	24.52 / 1.33	42.33 / 1.12
	Relation	10.26 / 0.29	23.72 / 0.34	41.47 / 0.39
CYCLO (2d - Ours)	Position	<b>13.71 / 0.85</b>	<b>26.07 / 1.45</b>	<b>43.94 / 1.49</b>
	Relation	<b>15.29 / 0.84</b>	<b>24.95 / 1.61</b>	<b>46.44 / 1.52</b>



## References

- [1] Songyou Peng, Kyle Genova, Chiyu Jiang, Andrea Tagliasacchi, Marc Pollefeys, Thomas Funkhouser, et al. Openscene: 3d scene understanding with open vocabularies. In *Proceedings of the IEEE/CVF Conference on Computer Vision and Pattern Recognition*, pages 815–824, 2023. 2
- [2] Yu-Huan Wu, Yun Liu, Xin Zhan, and Ming-Ming Cheng. P2t: Pyramid pooling transformer for scene understanding. *IEEE transactions on pattern analysis and machine intelligence*, 2022. 2
- [3] Jingwei Ji, Ranjay Krishna, Li Fei-Fei, and Juan Carlos Niebles. Action genome: Actions as compositions of spatio-temporal scene graphs. In *Proceedings of the IEEE/CVF Conference on Computer Vision and Pattern Recognition*, pages 10236–10247, 2020. 2, 4, 19, 20
- [4] Jingkang Yang, Wenxuan Peng, Xiangtai Li, Zujin Guo, Liangyu Chen, Bo Li, Zheng Ma, Kaiyang Zhou, Wayne Zhang, Chen Change Loy, et al. Panoptic video scene graph generation. In *Proceedings of the IEEE/CVF Conference on Computer Vision and Pattern Recognition*, pages 18675–18685, 2023. 2, 3, 4, 7, 8, 19, 20
- [5] Trong-Thuan Nguyen, Pha Nguyen, and Khoa Luu. Hig: Hierarchical interlacement graph approach to scene graph generation in video understanding. In *Proceedings of the IEEE/CVF Conference on Computer Vision and Pattern Recognition*, 2024. 2, 3, 4, 7, 19, 20
- [6] Xinpeng Liu, Yong-Lu Li, Xiaoqian Wu, Yu-Wing Tai, Cewu Lu, and Chi-Keung Tang. Interactiveness field in human-object interactions. In *Proceedings of the IEEE/CVF Conference on Computer Vision and Pattern Recognition*, pages 20113–20122, 2022. 2
- [7] Jeeseung Park, Jin-Woo Park, and Jong-Seok Lee. Viplo: Vision transformer based pose-conditioned self-loop graph for human-object interaction detection. In *Proceedings of the IEEE/CVF Conference on Computer Vision and Pattern Recognition*, pages 17152–17162, 2023. 2
- [8] Hanhua Ye, Guorong Li, Yuankai Qi, Shuhui Wang, Qingming Huang, and Ming-Hsuan Yang. Hierarchical modular network for video captioning. In *Proceedings of the IEEE/CVF Conference on Computer Vision and Pattern Recognition*, pages 17939–17948, 2022. 2, 3
- [9] Antoine Yang, Arsha Nagrani, Paul Hongsuck Seo, Antoine Miech, Jordi Pont-Tuset, Ivan Laptev, Josef Sivic, and Cordelia Schmid. Vid2seq: Large-scale pretraining of a visual language model for dense video captioning. In *Proceedings of the IEEE/CVF Conference on Computer Vision and Pattern Recognition*, pages 10714–10726, 2023. 2, 3
- [10] Wang Lin, Tao Jin, Ye Wang, Wenwen Pan, Linjun Li, Xize Cheng, and Zhou Zhao. Exploring group video captioning with efficient relational approximation. In *Proceedings of the IEEE/CVF International Conference on Computer Vision*, pages 15281–15290, 2023. 2, 3
- [11] Mahmoud Khademi and Oliver Schulte. Deep generative probabilistic graph neural networks for scene graph generation. In *Proceedings of the AAAI Conference on Artificial Intelligence*, volume 34, pages 11237–11245, 2020. 2, 3
- [12] Bruno Cesar de Oliveira Souza, Marius Aasan, Helio Pedrini, and Adin Ramirez Rivera. Selfgraphvqa: A self-supervised graph neural network for scene-based question answering. In *Proceedings of the IEEE/CVF International Conference on Computer Vision*, pages 4640–4645, 2023. 2, 3
- [13] Jian Ding, Nan Xue, Yang Long, Gui-Song Xia Xia, and Qikai Lu. Learning roi transformer for detecting oriented objects in aerial images. In *The IEEE Conference on Computer Vision and Pattern Recognition (CVPR)*, June 2019. 2, 3, 19
- [14] Pengfei Zhu, Longyin Wen, Dawei Du, Xiao Bian, Heng Fan, Qinghua Hu, and Haibin Ling. Detection and tracking meet drones challenge. *IEEE Transactions on Pattern Analysis and Machine Intelligence*, 44(11):7380–7399, 2021. 2, 3, 19
- [15] Aritra Dutta, Srijan Das, Jacob Nielsen, Rajat Subhra Chakraborty, and Mubarak Shah. Multiview aerial visual recognition (mavrec): Can multi-view improve aerial visual perception? In *Proceedings of the IEEE/CVF Conference on Computer Vision and Pattern Recognition*, 2023. 2, 3, 4, 19
- [16] Hao Zhang, Feng Li, Shilong Liu, Lei Zhang, Hang Su, Jun Zhu, Lionel Ni, and Heung-Yeung Shum. DINO: DETR with improved denoising anchor boxes for end-to-end object detection. In *The Eleventh International Conference on Learning Representations*, 2023. 2, 6, 7
- [17] Chang Xu, Jian Ding, Jinwang Wang, Wen Yang, Huai Yu, Lei Yu, and Gui-Song Xia. Dynamic coarse-to-fine learning for oriented tiny object detection. In *Proceedings of the IEEE/CVF Conference on Computer Vision and Pattern Recognition*, pages 7318–7328, 2023. 2
- [18] Xiang Yuan, Gong Cheng, Kebin Yan, Qinghua Zeng, and Junwei Han. Small object detection via coarse-to-fine proposal generation and imitation learning. In *Proceedings of the IEEE/CVF international conference on computer vision*, pages 6317–6327, 2023. 2

- [19] Yuren Cong, Wentong Liao, Hanno Ackermann, Bodo Rosenhahn, and Michael Ying Yang. Spatial-temporal transformer for dynamic scene graph generation. In *Proceedings of the IEEE/CVF international conference on computer vision*, pages 16372–16382, 2021. 2, 3, 4, 7
- [20] Chang Xu, Jinwang Wang, Wen Yang, Huai Yu, Lei Yu, and Gui-Song Xia. Detecting tiny objects in aerial images: A normalized wasserstein distance and a new benchmark. *ISPRS Journal of Photogrammetry and Remote Sensing*, 190:79–93, 2022. 3, 19
- [21] Gong Cheng, Jiabao Wang, Ke Li, Xingxing Xie, Chunbo Lang, Yanqing Yao, and Junwei Han. Anchor-free oriented proposal generator for object detection. *IEEE Transactions on Geoscience and Remote Sensing*, 60:1–11, 2022. 3, 19
- [22] Luigi Riz, Andrea Caraffa, Matteo Bortolon, Mohamed Lamine Mekhalfi, Davide Boscaini, André Moura, José Antunes, André Dias, Hugo Silva, Andreas Leonidou, et al. The monet dataset: Multimodal drone thermal dataset recorded in rural scenarios. In *Proceedings of the IEEE/CVF Conference on Computer Vision and Pattern Recognition*, pages 2545–2553, 2023. 3, 19
- [23] Gong Cheng, Xiang Yuan, Xiwen Yao, Kebin Yan, Qinghua Zeng, Xingxing Xie, and Junwei Han. Towards large-scale small object detection: Survey and benchmarks. *IEEE Transactions on Pattern Analysis and Machine Intelligence*, 2023. 2, 3, 19
- [24] Dawei Du, Yuankai Qi, Hongyang Yu, Yifan Yang, Kaiwen Duan, Guorong Li, Weigang Zhang, Qingming Huang, and Qi Tian. The unmanned aerial vehicle benchmark: Object detection and tracking. In *Proceedings of the European conference on computer vision (ECCV)*, pages 370–386, 2018. 2, 3, 19
- [25] Alexandre Robicquet, Amir Sadeghian, Alexandre Alahi, and Silvio Savarese. Learning social etiquette: Human trajectory understanding in crowded scenes. In *Computer Vision—ECCV 2016: 14th European Conference, Amsterdam, The Netherlands, October 11–14, 2016, Proceedings, Part VIII 14*, pages 549–565. Springer, 2016. 3, 19
- [26] Tung Minh Tran, Tu N Vu, Tam V Nguyen, and Khang Nguyen. Uit-adrone: A novel drone dataset for traffic anomaly detection. *IEEE Journal of Selected Topics in Applied Earth Observations and Remote Sensing*, 2023. 3, 19
- [27] Lichao Mou, Yuansheng Hua, Pu Jin, and Xiao Xiang Zhu. Era: A data set and deep learning benchmark for event recognition in aerial videos [software and data sets]. *IEEE Geoscience and Remote Sensing Magazine*, 8(4):125–133, 2020. 3, 4, 19
- [28] Murari Mandal, Lav Kush Kumar, and Santosh Kumar Vipparthi. Mor-uav: A benchmark dataset and baselines for moving object recognition in uav videos. In *Proceedings of the 28th ACM international conference on multimedia*, pages 2626–2635, 2020. 3, 19
- [29] Ilker Bozcan and Erdal Kayacan. Au-air: A multi-modal unmanned aerial vehicle dataset for low altitude traffic surveillance. In *2020 IEEE International Conference on Robotics and Automation (ICRA)*, pages 8504–8510. IEEE, 2020. 3, 19
- [30] Isha Kalra, Maneet Singh, Shruti Nagpal, Richa Singh, Mayank Vatsa, and PB Sujit. Dronesurf: Benchmark dataset for drone-based face recognition. In *2019 14th IEEE International Conference on Automatic Face & Gesture Recognition (FG 2019)*, pages 1–7. IEEE, 2019. 3, 19
- [31] Margherita Bonetto, Pavel Korshunov, Giovanni Ramponi, and Touradj Ebrahimi. Privacy in mini-drone based video surveillance. In *2015 11th IEEE international conference and workshops on automatic face and gesture recognition (FG)*, volume 4, pages 1–6. IEEE, 2015. 3, 19
- [32] Slim Hamdi, Samir Bouindour, Hichem Snoussi, Tian Wang, and Mohamed Abid. End-to-end deep one-class learning for anomaly detection in uav video stream. *Journal of Imaging*, 7(5):90, 2021. 3, 19
- [33] Ye Lyu, George Vosselman, Gui-Song Xia, Alper Yilmaz, and Michael Ying Yang. Uavid: A semantic segmentation dataset for uav imagery. *ISPRS journal of photogrammetry and remote sensing*, 165:108–119, 2020. 2, 3, 19
- [34] Ranjay Krishna, Yuke Zhu, Oliver Groth, Justin Johnson, Kenji Hata, Joshua Kravitz, Stephanie Chen, Yannis Kalantidis, Li-Jia Li, David A Shamma, et al. Visual genome: Connecting language and vision using crowdsourced dense image annotations. *International journal of computer vision*, 123:32–73, 2017. 2, 16, 19
- [35] Tao Wu, Runyu He, Gangshan Wu, and Limin Wang. Sportshhi: A dataset for human-human interaction detection in sports videos. In *Proceedings of the IEEE/CVF Conference on Computer Vision and Pattern Recognition*, 2024. 2, 19
- [36] Jingkan Yang, Jun Cen, Wenxuan Peng, Shuai Liu, Fangzhou Hong, Xiangtai Li, Kaiyang Zhou, Qifeng Chen, and Ziwei Liu. 4d panoptic scene graph generation. *Advances in Neural Information Processing Systems*, 36, 2024. 2
- [37] Jingkan Yang, Yi Zhe Ang, Zujin Guo, Kaiyang Zhou, Wayne Zhang, and Ziwei Liu. Panoptic scene graph generation. In *European Conference on Computer Vision*, pages 178–196. Springer, 2022. 3, 4, 19, 20, 22

- [38] Rongjie Li, Songyang Zhang, and Xuming He. Sgr: End-to-end scene graph generation with transformer. In *proceedings of the IEEE/CVF conference on computer vision and pattern recognition*, pages 19486–19496, 2022. 3
- [39] Zeeshan Hayder and Xuming He. Dsgg: Dense relation transformer for an end-to-end scene graph generation. In *Proceedings of the IEEE/CVF Conference on Computer Vision and Pattern Recognition*, 2024. 3
- [40] Jinbae Im, JeongYeon Nam, Nokyoung Park, Hyungmin Lee, and Seunghyun Park. Egtr: Extracting graph from transformer for scene graph generation. In *Proceedings of the IEEE/CVF Conference on Computer Vision and Pattern Recognition*, 2024. 3, 6
- [41] Sanjoy Kundu and Sathyanarayanan N Aakur. Is-ggt: Iterative scene graph generation with generative transformers. In *Proceedings of the IEEE/CVF Conference on Computer Vision and Pattern Recognition*, pages 6292–6301, 2023. 3
- [42] Kibum Kim, Kanghoon Yoon, Jaehyeong Jeon, Yeonjun In, Jinyoung Moon, Donghyun Kim, and Chanyoung Park. Llm4sgg: Large language model for weakly supervised scene graph generation. In *Proceedings of the IEEE/CVF Conference on Computer Vision and Pattern Recognition*, 2024. 3
- [43] Gege Gao, Weiyang Liu, Anpei Chen, Andreas Geiger, and Bernhard Schölkopf. Graphdreamer: Compositional 3d scene synthesis from scene graphs. *arXiv preprint arXiv:2312.00093*, 2023. 3
- [44] Yao Teng, Limin Wang, Zhifeng Li, and Gangshan Wu. Target adaptive context aggregation for video scene graph generation. In *Proceedings of the IEEE/CVF International Conference on Computer Vision*, pages 13688–13697, 2021. 3
- [45] Siddhesh Khandelwal and Leonid Sigal. Iterative scene graph generation. *Advances in Neural Information Processing Systems*, 35:24295–24308, 2022. 3, 4
- [46] Sayak Nag, Kyle Min, Subarna Tripathi, and Amit K Roy-Chowdhury. Unbiased scene graph generation in videos. In *Proceedings of the IEEE/CVF Conference on Computer Vision and Pattern Recognition*, pages 22803–22813, 2023. 3, 4
- [47] Mengze Li, Han Wang, Wenqiao Zhang, Jiaxu Miao, Zhou Zhao, Shengyu Zhang, Wei Ji, and Fei Wu. Winner: Weakly-supervised hierarchical decomposition and alignment for spatio-temporal video grounding. In *Proceedings of the IEEE/CVF Conference on Computer Vision and Pattern Recognition*, pages 23090–23099, 2023. 3
- [48] Chaolei Tan, Zihang Lin, Jian-Fang Hu, Wei-Shi Zheng, and Jianhuang Lai. Hierarchical semantic correspondence networks for video paragraph grounding. In *Proceedings of the IEEE/CVF Conference on Computer Vision and Pattern Recognition*, pages 18973–18982, 2023. 3
- [49] Zihang Lin, Chaolei Tan, Jian-Fang Hu, Zhi Jin, Tiancai Ye, and Wei-Shi Zheng. Collaborative static and dynamic vision-language streams for spatio-temporal video grounding. In *Proceedings of the IEEE/CVF Conference on Computer Vision and Pattern Recognition*, pages 23100–23109, 2023. 3
- [50] Yao-Hung Hubert Tsai, Santosh Divvala, Louis-Philippe Morency, Ruslan Salakhutdinov, and Ali Farhadi. Video relationship reasoning using gated spatio-temporal energy graph. In *Proceedings of the IEEE/CVF Conference on Computer Vision and Pattern Recognition*, pages 10424–10433, 2019. 3
- [51] Xufeng Qian, Yueting Zhuang, Yimeng Li, Shaoning Xiao, Shiliang Pu, and Jun Xiao. Video relation detection with spatio-temporal graph. In *Proceedings of the 27th ACM international conference on multimedia*, pages 84–93, 2019. 3
- [52] Xindi Shang, Yicong Li, Junbin Xiao, Wei Ji, and Tat-Seng Chua. Video visual relation detection via iterative inference. In *Proceedings of the 29th ACM international conference on Multimedia*, pages 3654–3663, 2021. 3, 4
- [53] Jingwei Ji, Ranjay Krishna, Fei-Fei Li, and Juan Carlos Niebles. Action genome: Actions as compositions of spatio-temporal scene graphs. In *CVPR*, 2020. 3
- [54] Jiahao Wang, Guo Chen, Yifei Huang, Limin Wang, and Tong Lu. Memory-and-anticipation transformer for online action understanding. In *Proceedings of the IEEE/CVF International Conference on Computer Vision*, pages 13824–13835, 2023. 4
- [55] Shuqiang Cao, Weixin Luo, Bairui Wang, Wei Zhang, and Lin Ma. A circular window-based cascade transformer for online action detection. *arXiv preprint arXiv:2208.14209*, 2022. 4
- [56] Nicolas Carion, Francisco Massa, Gabriel Synnaeve, Nicolas Usunier, Alexander Kirillov, and Sergey Zagoruyko. End-to-end object detection with transformers. In *European conference on computer vision*, pages 213–229. Springer, 2020. 6
- [57] Ashish Vaswani, Noam Shazeer, Niki Parmar, Jakob Uszkoreit, Llion Jones, Aidan N Gomez, Łukasz Kaiser, and Illia Polosukhin. Attention is all you need. *Advances in neural information processing systems*, 30, 2017. 6, 20

- [58] Thanh-Dat Truong, Quoc-Huy Bui, Chi Nhan Duong, Han-Seok Seo, Son Lam Phung, Xin Li, and Khoa Luu. Direcformer: A directed attention in transformer approach to robust action recognition. In *Proceedings of the IEEE/CVF Conference on Computer Vision and Pattern Recognition*, pages 20030–20040, 2022. 6
- [59] Cewu Lu, Ranjay Krishna, Michael Bernstein, and Fei-Fei Li. Visual relationship detection with language priors. In *ECCV*, 2016. 8
- [60] Shilong Zhang, Peize Sun, Shoufa Chen, Min Xiao, Wenqi Shao, Wenwei Zhang, Kai Chen, and Ping Luo. Gpt4roi: Instruction tuning large language model on region-of-interest. *arXiv preprint arXiv:2307.03601*, 2023. 15
- [61] Tsung-Yi Lin, Michael Maire, Serge Belongie, James Hays, Pietro Perona, Deva Ramanan, Piotr Dollár, and C Lawrence Zitnick. Microsoft coco: Common objects in context. In *Computer Vision—ECCV 2014: 13th European Conference, Zurich, Switzerland, September 6–12, 2014, Proceedings, Part V 13*, pages 740–755. Springer, 2014. 16
- [62] Lianmin Zheng, Wei-Lin Chiang, Ying Sheng, Siyuan Zhuang, Zhanghao Wu, Yonghao Zhuang, Zi Lin, Zhuohan Li, Dacheng Li, Eric Xing, Hao Zhang, Joseph E. Gonzalez, and Ion Stoica. Judging LLM-as-a-judge with MT-bench and chatbot arena. In *Thirty-seventh Conference on Neural Information Processing Systems Datasets and Benchmarks Track*, 2023. 16
- [63] Hugo Touvron, Thibaut Lavril, Gautier Izacard, Xavier Martinet, Marie-Anne Lachaux, Timothée Lacroix, Baptiste Rozière, Naman Goyal, Eric Hambro, Faisal Azhar, et al. Llama: Open and efficient foundation language models. *arXiv preprint arXiv:2302.13971*, 2023. 16
- [64] Danfei Xu, Yuke Zhu, Christopher B Choy, and Li Fei-Fei. Scene graph generation by iterative message passing. In *Proceedings of the IEEE conference on computer vision and pattern recognition*, pages 5410–5419, 2017. 19
- [65] Yuanzhi Liang, Yalong Bai, Wei Zhang, Xueming Qian, Li Zhu, and Tao Mei. Vrr-vg: Refocusing visually-relevant relationships. In *Proceedings of the IEEE/CVF international conference on computer vision*, pages 10403–10412, 2019. 19
- [66] Drew A Hudson and Christopher D Manning. Gqa: A new dataset for real-world visual reasoning and compositional question answering. In *Proceedings of the IEEE/CVF conference on computer vision and pattern recognition*, pages 6700–6709, 2019. 19
- [67] Xindi Shang, Tongwei Ren, Jingfan Guo, Hanwang Zhang, and Tat-Seng Chua. Video visual relation detection. In *Proceedings of the 25th ACM international conference on Multimedia*, pages 1300–1308, 2017. 19
- [68] Xindi Shang, Donglin Di, Junbin Xiao, Yu Cao, Xun Yang, and Tat-Seng Chua. Annotating objects and relations in user-generated videos. In *Proceedings of the 2019 on International Conference on Multimedia Retrieval*, pages 279–287, 2019. 19
- [69] Zhu Zhang, Zhou Zhao, Yang Zhao, Qi Wang, Huasheng Liu, and Lianli Gao. Where does it exist: Spatio-temporal video grounding for multi-form sentences. In *Proceedings of the IEEE/CVF Conference on Computer Vision and Pattern Recognition*, pages 10668–10677, 2020. 19
- [70] Dima Damen, Hazel Doughty, Giovanni Maria Farinella, Antonino Furnari, Evangelos Kazakos, Jian Ma, Davide Moltisanti, Jonathan Munro, Toby Perrett, Will Price, et al. Rescaling egocentric vision: Collection, pipeline and challenges for epic-kitchens-100. *International Journal of Computer Vision*, pages 1–23, 2022. 19
- [71] Kaiming He, Georgia Gkioxari, Piotr Dollár, and Ross Girshick. Mask r-cnn. In *Proceedings of the IEEE international conference on computer vision*, pages 2961–2969, 2017. 21

# Appendices

## A The AeroEye Dataset

### A.1 Relationship Definition

Our AeroEye dataset focuses on capturing the spatial positions and relationships between objects, including person-to-object and object-to-object interactions. Table A.8, A.9 provide a comprehensive list of the defined positions and relationships. Furthermore, Table A.10 offers guidance on the final relationship vocabulary specific to each scene category within the dataset.

Table A.8: A list of the 135 position predicates defined on the AeroEye dataset.

above	at focal points	near playground equipment
above debris	at intersection	near safe exits
above water lines	at the ends of the pool	near scoring zones
across different terrains	at the forefront of movements	near storage areas
across multiple lanes	at the helm	next to
across negotiation tables	at the junction	on benches
across ploughed fields	at the starting line	opposite
across the court	at the stern or sides	oriented
across the site	at turning point	outside
adjacent to	behind	outside danger zones
ahead in the race	behind agricultural machinery	outside of traffic flow
ahead of competitors	behind the congregation	over
aligned on the track	below unstable hillsides	over open waters
along a designated route	beneath	parallel
along cleared pathways	beside	parallel in lanes
along docks and aboard ships	beside bike lanes	surrounding the field
along monitored sections	beside debris	through city streets
along paths	beside merchandise stands	through debris
along pit stops	beside pool edges	through rows of crops
along roads	beside the congregation	throughout the fields
along the field	between	to the left
along the route	between buildings	to the right
along the sidelines	between conflicting parties	together
along the sides	between crop rows	under
along the sides of the pool	centered	undergoing
along viewing areas or walkways	close by	underneath
alongside construction machinery	close to	within affected zones
amidst debris	closely positioned	within audience clusters
angled	clustered	within bottleneck points
around campus landmarks	distant	within cabin areas
around common areas	down	within crash sites
around damaged structures	facing	within crowd formations
around familiar objects	facing the audience	within dance areas
around heavy equipment	facing the stage	within debris piles
around penalty boxes	from a vantage point	within designated lanes
around refreshment tables	from central points	within discussion circles
around ritual objects	from control centers	within goal areas
around stage areas	in designated pit areas	within marked lanes
around temporary aid stations	in front of	within moored boats
around the deck	in lane	within open fields
around the fire	indifferent	within outfield areas
around the vehicles	inside	within reach of fire hydrants
around water features	interwoven	within spectator areas
at a safe distance	near	within surveillance zones
at batting positions	near debris	within the basketball court



Table A.9: A list of the 249 relationship predicates defined on the AeroEye dataset.

acquaintances	dribbling	leading the way	riding
adhering to	drivers	learning	runners
alerting	encircled by	learning about farming	running
aligned in traffic lane	encircling	living in coastal community	scoring
aligned movement	enclosed	loading	selling
aligning in lane	engaging in beach sports	loading cargo onto ship	selling merchandise
along sidewalk	engaging in leisure activity	managing airport operations	setting up
along the lane	engaging in school sports	managing industrial operations	setting up temporary shelters
along the road	engaging in winter activities	managing urban traffic	sharing lane
along the sidewalk	enjoying concert atmosphere	merging lane	sharing slogans
amidsting traffic	enjoying lakeside park	mimicking	sharing their excitement
appreciating art exhibits	enjoying live music	monitoring	shopping
approaching	enjoying outdoor cinema	motivating	shopping in city
approaching intersection	enjoying outdoor festivities	moving	showcasing classic car
at center of intersection	enjoying spring festivities	moving at intersection	showcasing local art
at the conjunction	enjoying waterfront gathering	moving towards	singing
at the stop sign	enjoying wilderness	navigating	skating
attending games	enjoying winter recreation	negotiating	skiing
boarding	enjoying winter sports	observing	socializing
boaters	entertaining outdoor crowd	operating in docking area	standing inside
bordering	excavating	operating market stalls	standing outside
building coastal protection	exchanging	opponents	stopping at
building team cohesion	exercising	overlooking	straddling lanes
building underwater structure	exploring forest trails	overtaking	surrounded by
building urban infrastructure	exploring mountain trails	owner	swimmers
camping	exploring urban landscapes	painting	tackling
capturing	exploring wildlife habitat	parallel	teammates
capturing urban night lights	external to the building	parking at	tending to agricultural tasks
catching	extinguishing	participating in community event	touring
celebrating	farmer and harvesting tool	participating in festivities	toward destination
celebrating in festive atmosphere	farmers	participating in marathon	towing
celebrating public festival	finding parking lot	participating in music camp	tracking
changing direction	firefighters	partners	trading
chasing	floating	passing	training
cheering	following behind	performing	traveling
cleaning	forefronted	picnicking together	traversing
close friends	friends	players	trying to mediate resolutions
co-traveling	friends dancing together	playing	under observation
coaching	gathering	polices	under surveillance
coincidental	graduating	practicing	undergoing
collaborating	handling emergency	preparing for emergencies	undergoing process
collecting crops	handling the plough	preserving beautiful moments	unloading
collecting soil samples	harvesting	preserving natural resources	utilizing riverside path
colliding	heading	protecting waterways	vacationing in resort
communicating	heading towards	protesters	viewing
competing	helping	providing aid	visiting
conserving marine environment	hiking	racers	visiting historical landmarks
constructing	hindering	racing in adventure challenge	waiting at light
contiguous	homeowner and damaged property	racing through city streets	walking
cooperating	hosting lakeside wedding	racing through mountain trails	watching
coordinated in lane	hosting outdoor concert	raising awareness and funds	watching wildlife
coordinating	in conflict	rear	within parking area
coordinating logistics	in line	reconstructing	within traffic zone
crashing	in the middle	reenacting	worker and construction tools
crossing	independent	regulated movement	workers
cyclists	inside construction zone	relaxing	working
debating	inspecting	repairing	worshippers
demonstrating	installing	resident and mudslide debris	serving food
directing along	interacting	residents evacuating together	pitching
directing toward	investigating	responding	hosting rest stop
discussing	isolated during flood	resting	
displaying	kicking	retrieving	
distributing	lead	revamping urban area	

## A.2 Annotation Pipeline

To capture frequent and rapid changes in aerial videos while reducing redundancy, we annotate keyframes at 5FPS. At each frame, our annotation pipeline consists of two stages:

**Stage 1: Object Localization and Tracking.** We manually annotate bounding boxes with predefined categories, providing precise object localization and consistent tracking throughout the video.

**Stage 2: Relationship Instance Annotation.** To generate diverse predicates, we leverage the GPT4RoI [60] model, which combines visual and linguistic data to generate detailed descriptions of object relationships within specified regions of interest. The process involves the following steps:

Table A.10: A hierarchical representation of the 249 relationship predicates on the AeroEye dataset, organized into 29 high-level semantic scene categories.

Scene	Relationship Predicates
Baseball	cheering, watching, players, competing, passing, scoring
Basketball	cheering, watching, players, competing, dribbling, passing
Boating	floating, boaters, navigating, enjoying waterfront gathering
Campus	studying, engaging in school sports, learning, graduating
Car Racing	racing through city streets, drivers, overtaking, moving
Concert	enjoying concert atmosphere, cheering, watching, participating in community event
Conflict	in conflict, debating, trying to mediate resolutions, responding
Constructing	building urban infrastructure, inside construction zone, worker and construction tools, workers, working, inspecting, installing
Cycling	moving, traveling, riding, cyclists, navigating, along the road
Fire	extinguishing, responding, firefighters, isolated during flood
Flood	rescuing, responding, isolated during flood, floating
Harbour	loading cargo onto ship, operating in docking area, floating, navigating
Harvesting	collecting crops, farmers, harvesting, tending to agricultural tasks
Landslide	rescuing, responding, homeowner and damaged property, isolated during flood, managing industrial operations
Mudslide	rescuing, responding, homeowner and damaged property, undergoing process, managing industrial operations
NonEvent	isolated during flood, observing, under surveillance
Parade Protest	demonstrating, sharing slogans, in line, participating in community event
Park	picnicking together, enjoying lakeside park, engaging in leisure activity, walking
Party	celebrating, socializing, enjoying outdoor festivities, dancing, singing
Ploughing	tending to agricultural tasks, farmers, moving along the lane
Police Chase	chasing, responding, following behind, in conflict, moving at intersection
Post Earthquake	rescuing, responding, reconstructing, homeowner and damaged property
Religious Activity	worshippers, engaging in leisure activity, participating in community event
Running	moving, traveling, navigating, runners, participating in marathon
Soccer	cheering, watching, players, competing, passing, scoring, kicking, marking
Swimming	enjoying lakeside park, enjoying waterfront gathering, swimmers, floating, tackling
Traffic Collision	approaching, crashing, responding, colliding, drivers, in the middle of intersection
Traffic Congestion	approaching, drivers, waiting at light, along the road, sharing lane
Traffic Monitoring	approaching, monitoring, managing urban traffic, observing, under surveillance

1. **Text Generation:** We leverage GPT4RoI integrated instruction tuning with a large language model (LLM) to enhance interactions with regions of interest (RoI) within images. This model transforms bounding box references into language instructions, enabling detailed descriptions and reasoning about specific image regions, thus improving image understanding granularity and accuracy. It utilizes a variety of transformed multimodal datasets, including COCO [61] and Visual Genome [34], to refine the alignment between visual and linguistic data, ensuring precise responses to spatial queries.

In particular, We input bounding boxes around objects with prompts such as, "What is the relationship between <object\_1> in <region\_1> and <object\_2> in <region\_2>?", where <object\_1> is a category name that labeled in Stage 1, and GPT4RoI replaces <region\_1> tags in these instructions with results from RoIAlign, derived directly from the features of image. The model uses RoIAlign to extract region-specific features and combine them with language embeddings. The resulting multimodal embeddings are then interpreted by the Vicuna model [62], an instance of LLaMA [63].

2. **Predicate Summarization and Selection:** We employ a custom-designed filter to categorize the generated text into relationship types. This filter utilizes a combination of keyword matching, dependency parsing, and semantic analysis to identify and classify the predicates accurately. The filter is designed to handle sentence structure and terminology variations, ensuring that the identified predicates are correctly mapped to their corresponding relationship types. Furthermore, the filter incorporates a confidence scoring mechanism to prioritize high-quality predicates and filter out irrelevant or ambiguous ones. The final selection of predicates undergoes human oversight, where experienced annotators review and validate the filtered results. This manual verification step ensures the highest accuracy and relevance of the identified predicates, mitigating potential errors introduced by automated processing.

**Quality Control** To maintain the highest standard of annotation quality, we implement the following comprehensive measures:

- Stage 1: Object Localization and Tracking:
  - All bounding box annotations are performed manually by skilled annotators, without relying on automated detection or tracking models. This ensures precise object localization tailored to the specific characteristics of aerial videos.

- We employ a rigorous double-checking process, where each frame in every video is carefully reviewed by a second annotator. This step helps identify and rectify any inaccuracies in bounding box placement or dimensions.
- In cases where object identities are inconsistent across frames due to occlusion, visual similarity, or other challenges, annotators meticulously correct the object numbers to maintain consistent tracking throughout the video.
- Stage 2: Relationship Instance Annotation:
  - Annotators undergo extensive training using carefully curated examples from previous VidSGG datasets. This training familiarizes them with the intricacies of extracting predicates generated by the LLM and ensures a deep understanding of the annotation guidelines and best practices.
  - To minimize individual biases and ensure the robustness of annotations, we implement a repeated annotation process. Each video is distributed to multiple annotators, who independently extract and record the relationship instances. This redundancy allows for cross-validation and helps identify potential discrepancies or ambiguities.
  - In cases where annotators disagree on the extracted predicates or their categorization, a highly experienced meta-annotator is assigned to review the conflicting annotations. The meta-annotator carefully examines the video content, considers the perspectives of the individual annotators, and makes the final decision on the annotation record. This hierarchical review process ensures consistency and accuracy across the dataset.

By employing these rigorous quality control measures at each stage of the annotation pipeline, we ensure the highest level of *accuracy*, *consistency*, and *completeness* in relationship instances.

### A.3 Data Format

Our annotations are stored in JSON (JavaScript Object Notation) format organized as below:

---

```

1 data[{
2   "file_name": str,
3   "height": int,
4   "width": int,
5   "image_id": int,
6   "frame_index": int,
7   "video_id": int,
8   "metadata": [{
9     "id": int,
10    "category_id": int,
11    "iscrowd": 0 or 1,
12    "area": int
13  }],
14  "annotations": [{
15    "bbox": [x, y, width, height],
16    "bbox_mode": 0 or 1,
17    "category_id": int,
18    "track_id": int
19  }],
20  "positions": [[
21    metadata_id,
22    metadata_id,
23    position_id
24  ]],
25  "relations": [[
26    metadata_id,
27    metadata_id,
28    relation_id
29  ]]
30 }],
31 "categories": {

```

```

32     "id": int,
33     "name": str
34 },
35 "predicate_positions": {
36     "id": int,
37     "name": str
38 },
39 "predicate_relations": {
40     "id": int,
41     "name": str
42 }

```

---

**Basic Image Information.** This section contains the fundamental attributes of each image:

- `file_name` (str): The name of the image file.
- `height` (int): The height of the image in pixels.
- `width` (int): The width of the image in pixels.
- `image_id` (int): A unique identifier for the image.
- `frame_index` (int): The index of the frame within the video sequence.
- `video_id` (int): An identifier for the video to which this image/frame belongs.

**Metadata.** This section includes the `metadata` key, which is a list of segments within the image. Each segment contains:

- `id` (int): Unique identifier for the segment.
- `category_id` (int): Identifier for the category of the object in the segment.
- `iscrowd` (0 or 1): 0 for a single object and 1 for a cluster of objects.
- `area` (int): The area covered by the segment in the image.

The `annotations` key contains a list of corresponding bounding boxes for each entry in `metadata`, each tagged with a specific `category_id`:

- `bbox` (list): [`x_center`, `y_center`, `width`, `height`] of the bounding box.
- `bbox_mode` (0 or 1): Bounding box mode.
- `category_id` (int): Identifier for the object category in the bounding box.
- `track_id` (int): Identifier to track the bounding box across different frames.

**Relationship Attributes.** This section encompasses lists of `positions` and `relations` for each segment, including two different `metadata_ids` to represent the interactivity between two segments:

- `positions` (list): List of position relations between segments, each containing:
  - `metadata_id` (int): Identifier for the first segment.
  - `metadata_id` (int): Identifier for the second segment.
  - `position_id` (str): Identifier for position relation between the segments.
- `relations` (list): List of other relations between segments, each containing:
  - `metadata_id` (int): Identifier for the first segment.
  - `metadata_id` (int): Identifier for the second segment.
  - `relation_id` (str): Identifier for relationship between the segments.

These descriptors represent lists specifying various subject, object, and interactivity aspects for each bounding box within the annotations and metadata. For example, [3, 0, 5] indicates that the third and first metadata segments share the relationship with an ID of 5.

Table A.11: Comparison of available datasets for scene graph generation. The top two blocks present image and video scene graph datasets, while the next two focus on image and drone video datasets. Viewpoints include five types: from ego (1st-person) view to 3rd-person view, and drone-captured perspectives, which is our main focus in this work (✓/✗ in colors), including **aerial** (top-down), **oblique** (slanted), and **ground** (eye-level) perspectives. # denotes the number of corresponding items. The best values in *drone* blocks are **highlighted**.

Datasets	#Videos	#Frames	Resolution	Annotations			#ObjCls	#RelCls	#Scenes	Viewpoints				
				BBox	Relation	#Instances				3rd	ego	aerial	oblique	ground
Visual Genome [34]	-	108K	-	✓	✓	3.8M	33K	42K	-	✓	✗	✗	✗	✗
VG-150 [64]	-	88K	-	✓	✓	2.8M	150	50	-	✓	✗	✗	✗	✗
VrR-VG [65]	-	59K	-	✓	✓	282.4K	1.6K	117	-	✓	✗	✗	✗	✗
GQA [66]	-	85K	-	✓	✓	-	1.7K	310	-	✓	✗	✗	✗	✗
PSG [37]	-	49K	-	✓	✓	538.2K	80	56	-	✓	✗	✗	✗	✗
VidVRD[67]	1K	<b>296.2K</b>	<b>1920 × 1080</b>	✓	✓	15.1K	35	132	-	✓	✗	✗	✗	✗
Action Genome [3]	<b>10K</b>	234.3K	1280 × 720	✓	✓	<b>476.3K</b>	25	25	-	✓	✗	✗	✗	✗
ASPIRe [5]	1.5K	1.6M	1280 × 720	✓	✓	167.8K	<b>833</b>	<b>4.5K</b>	<b>7</b>	✓	✗	✗	✗	✗
SportsHHI [35]	80	11.4K	1280 × 720	✓	✓	118.1K	1	34	2	✓	✗	✗	✗	✗
VidOR [68]	<b>10K</b>	55.4	640 × 360	✓	✓	50K	80	50	1	✓	✗	✗	✗	✗
VidSTG [69]	<b>10K</b>	55.4	640 × 360	✓	✓	50K	80	50	1	✓	✗	✗	✗	✗
EPIC-KITCHENS [70]	700	11.5K	<b>1920 × 1080</b>	✓	✓	454.3K	21	13	1	✓	✓	✗	✗	✗
PVSG [4]	400	153K	<b>1920 × 1080</b>	✓	✓	7.6K	126	57	<b>7</b>	✓	✓	✗	✗	✗
DOTA [13]	-	11.3K	1490 × 957	✓	✗	1.8M	18	-	-	✗	✗	✓	✗	✗
AI-TOD [20]	-	28.1K	800 × 800	✓	✗	700.6K	8	-	-	✗	✗	✓	✗	✗
DIOR-R [21]	-	23.5K	800 × 800	✓	✗	192.5K	<b>20</b>	-	-	✗	✗	✓	✗	✗
MONET [22]	-	<b>53K</b>	-	✓	✗	162K	3	-	-	✗	✗	✓	✗	✗
SODA-A [23]	-	2.5K	<b>4761 × 2777</b>	✓	✗	<b>872.1K</b>	9	-	-	✗	✗	✓	✗	✓
VisDrone [14]	288	261.9K	3840 × 2160	✓	✗	<b>2.6M</b>	<b>10</b>	-	-	✗	✗	✓	✗	✗
UAVDT [24]	100	40.7K	1080 × 540	✓	✗	0.84M	3	-	6	✗	✗	✓	✗	✗
Stanford Drone [25]	<b>10K</b>	<b>929.5K</b>	-	✓	✗	-	6	-	8	✗	✗	✓	✗	✗
UIT-ADrone [26]	51	206.2K	1920 × 1080	✓	✗	210.5K	8	-	1	✗	✗	✓	✗	✗
ERA [27]	2.9K	343.7K	640 × 640	✓	✗	-	-	-	<b>25</b>	✗	✗	✓	✗	✗
MOR-UAV [28]	30	10.9K	1920 × 1080	✓	✗	89.8K	2	-	-	✗	✗	✓	✗	✗
AU-AIR [29]	-	32.8K	1920 × 1080	✓	✗	132K	8	-	-	✗	✗	✓	✗	✗
DroneSURF [30]	200	411.5K	1280 × 720	✓	✗	786K	1	-	-	✗	✗	✓	✗	✗
MiniDrone [31]	38	23.3K	224 × 224	✓	✗	-	-	-	1	✗	✗	✓	✗	✗
Brutal Running [32]	-	1K	227 × 227	✓	✗	-	-	-	1	✗	✗	✓	✗	✗
UAVid [33]	30	300	<b>4096 × 2160</b>	✓	✗	-	8	-	-	✗	✗	✓	✗	✗
MAVREC [15]	24	537K	3840 × 2160	✓	✗	1.1M	<b>10</b>	-	4	✗	✗	✓	✗	✓
AeroEye (Ours)	<b>2.3K</b>	<b>261.5K</b>	<b>3840 × 2160</b>	✓	✓	<b>1.8M</b>	<b>57</b>	<b>384</b>	<b>29</b>	✗	✗	✓	✓	✓

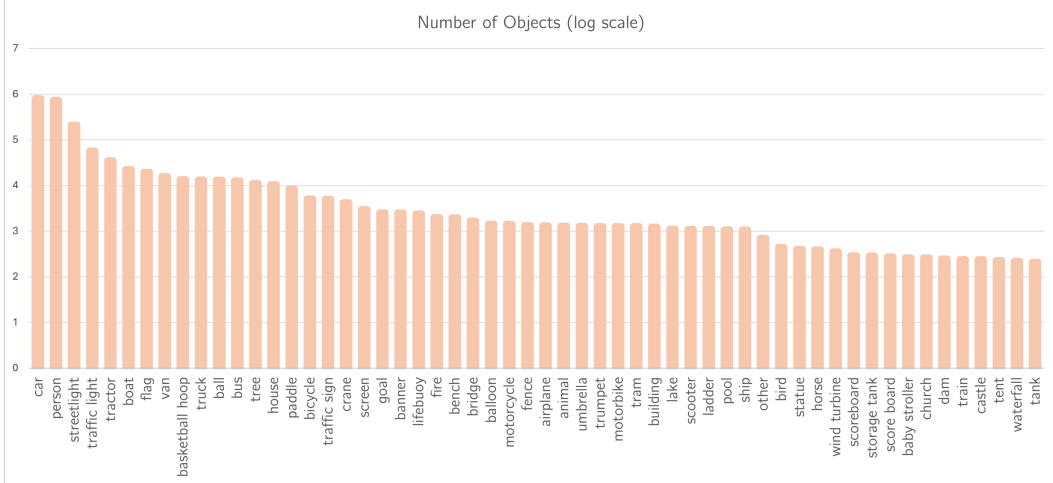


Figure A.8: Distribution of objects per category on the AeroEye dataset.

#### A.4 Additional Statistics

We present object, position, and relationship statistics per category in Fig. A.8, A.9, and A.10.

#### A.5 Data Samples

Fig. A.11 presents selected samples from our *AeroEye* dataset, distinguished by its detailed bounding box annotations and meticulous relationship descriptions across various scenarios. As outlined in Section 3.2, each frame within AeroEye is annotated with precision and contextual relevance, ensuring clarity and avoiding the common ambiguities, such as generic or overlapping labels, prevalent in other





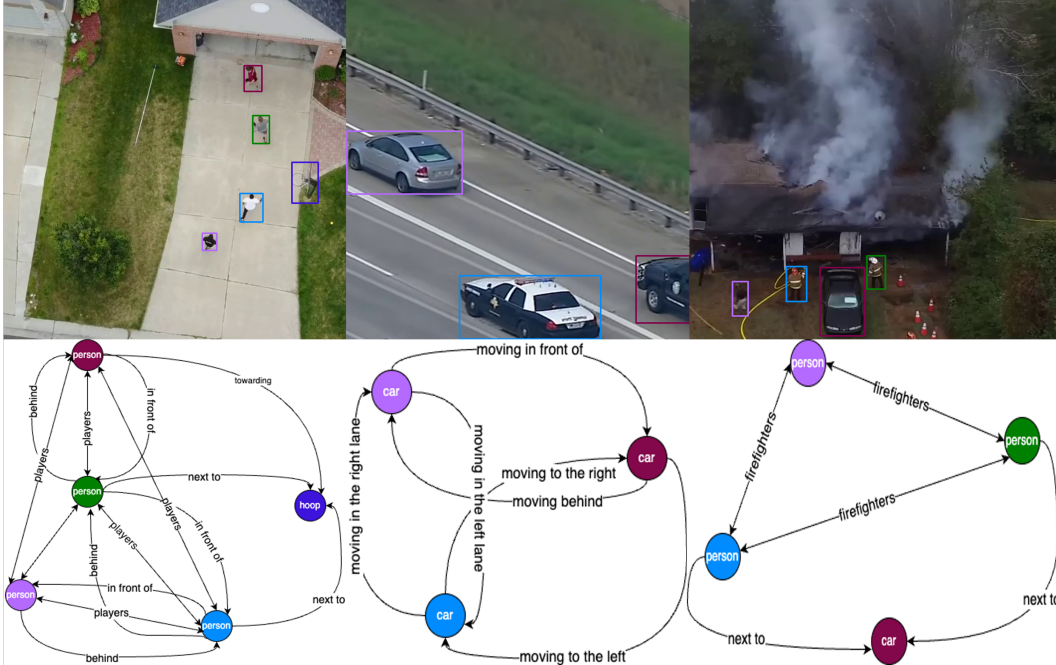


Figure A.11: Our *AeroEye* dataset includes a diverse range of scenarios, objects, and relationships.

Finally, the multi-head attention output is normalized, passed through a feed-forward network, and normalized again with a residual connection to form a complete transformer layer.

## B.2 Concepts

### B.2.1 Progression

**Relationship Representation.** In each frame, a detector provides to a set of object features  $\{\hat{v}_t^1, \dots, \hat{v}_t^{N(t)}\}$ , bounding boxes  $\{\hat{b}_t^1, \dots, \hat{b}_t^{N(t)}\}$ , and category distributions  $\{\hat{d}_t^1, \dots, \hat{d}_t^{N(t)}\}$  for the detected objects. These elements are used to define the relationships  $\hat{x}_t^k$ :

$$\hat{x}_t^k = \left[ \phi_{W_s} \hat{z}_i^t, \phi_{W_o} \hat{z}_j^t, \phi_{W_u} \varphi(\hat{u}_t^{ij} \odot f(\hat{b}_i^t, \hat{b}_j^t)), \hat{s}_i^t, \hat{s}_j^t \right] \quad (\text{B.9})$$

where  $[\cdot, \cdot]$  denotes concatenation,  $\varphi$  denotes a flattening operation,  $\odot$  represents element-wise addition, and the linear transformation matrices  $\phi_{W_s}$ ,  $\phi_{W_o}$ , and  $\phi_{W_u}$ .  $\hat{u}_t^{ij}$  implies the feature map of the union box, computed by the RoIAlign [71], while  $f$  is a function that converts the bounding boxes of the subject  $\hat{b}_i^t$  and object  $\hat{b}_j^t$  into a feature map with the same dimensions as  $\hat{u}_t^{ij}$ . The semantic embedding vectors  $\hat{s}_i^t$  and  $\hat{s}_j^t$  are obtained from the object categories  $\hat{c}_i^t$  and  $\hat{c}_j^t$ , respectively.

In the progressive approach, features  $v_t^i$  for each object are obtained using a detector such as Faster R-CNN in each frame. These features are utilized as specified in Eqn. (B.9) to compute the relationship features  $\hat{x}_t^k$ . Finally, these features are processed through multilayer perceptions (MLPs) followed by softmax activation functions to classify the types of relationships between objects.

### B.2.2 Batch Progression

In contrast to the Progressive approach, the Batch Progressive approach passes the relationship features through a Transformer architecture (detailed in Appendix B.1) before classification.

A set of relationship features  $\hat{X}_t = \{\hat{x}_t^1, \hat{x}_t^2, \dots, \hat{x}_t^{K(t)}\}$  is fed into the Transformer *Encoder*, which focuses on understanding the spatial context by inputting these relationship features into a sequence of identical self-attention layers, defined as:

$$\hat{X}_t^{(n)} = \text{Att}_{\text{enc.}}(Q = K = V = \hat{X}_t^{(n-1)}) \quad (\text{B.10})$$

Each  $n$ -th layer receives the output from the  $(n-1)$ -th layer as its input, iteratively refining to enhance the representation of spatial relations embedded in the features, where  $n$  denotes the layer number. The outputs are then processed by the **Decoder**, which captures temporal dependencies between frames, applying a sliding window over the sequence of spatially contextualized representations:

$$\widehat{Z}_i = [\widehat{X}_i, \dots, \widehat{X}_{T-\eta-1}], \quad i \in \{1, \dots, T\} \quad (\text{B.11})$$

where  $\eta$  is the window size, and  $T$  is number of frames. The positional encoding  $E_f = [e_1, \dots, e_\eta]$  is embedded into the input to maintain sequence order:

$$Q = K = \widehat{Z}_i + E_f, V = \widehat{Z}_i, Z_i = \text{Att}_{\text{dec.}}(Q, K, V). \quad (\text{B.12})$$

Equation (B.12) enables the decoder to process each batch using self-attention layers, combining relation representations  $\widehat{Z}_i$  with positional encodings  $E_f$ .

### B.2.3 Hierarchical Graph

The hierarchical interlacement graph (HIG) method abstracts video content by representing temporal relationships using a multi-level graph structure. Higher-level graph cells encompass broader segments of video frames, allowing the HIG to efficiently capture and model the temporal dependencies and connections across different time scales within the video. In this method, object features  $\widehat{v}_t^i$  from individual frames are spatially and temporally fused to form graph nodes. These nodes are interconnected across successive frames, resulting in a series of interconnected frame-based graphs  $\{G_t(V_t, E_t)\}_{t=1}^T$ , where each  $G_t$  is defined by its vertices  $V_t$  and edges  $E_t$ . As the graph traverses, the total number of graphs decreases, ultimately resulting in a singular graph representing the entire video. This hierarchical graph operates on predefined hierarchical levels  $L$ . At each level  $l$ , the temporal scope is adjusted to  $T_l = T - l + 1$ , and a new graph is generated that is specific to that level and timeframe. Therefore, node features within each graph are dynamically updated through the computation and aggregation of messages from adjacent nodes, computed by weight matrices for each level  $l$  and node pair  $(\widehat{v}_i, \widehat{v}_j)$ . This iterative refinement process is applied across all levels, resulting in a consolidated graph structure and updated feature set. Finally, relationship features between each node pair  $(\widehat{v}_i, \widehat{v}_j)$  are fused and analyzed to classify the relationships.

### B.3 Baseline Methods

In the experiments shown in Table 6 and Table 7, we compare our method with four baseline approaches introduced in [37]. The Vanilla approach, also known as the Progressive approach, and the 1D Convolution, Handcrafted, and Transformer approaches are all considered Batch Progressive methods. The Vanilla and Transformer approaches are described in more detail in Section B.2. The Handcrafted and 1D-Convolutional approaches are introduced below:

**Handcrafted.** To incorporate temporal information effectively, the handcrafted filter is designed to integrate context from adjacent frames, enhancing the temporal coherence in feature representation. The filter (*e.g.*, Gaussian), applied across the temporal dimension of the feature vectors:

$$h_t^k = \sum_{i=-W/2}^{W/2} g_i \cdot x_{t+i}^k \quad (\text{B.13})$$

where  $x_t^k$  represents the feature vector,  $W$  is the kernel size, and  $w_i$  are the learnable weights. The weights  $w_i$  are defined by the vector  $[1/4, 1/2, 1, 1/2, 1/4]$  with a window size of 5 frames.

**1D-Convolutional.** A learnable 1D-Convolutional layer uses CNN consisting of three 1D convolutional layers with a kernel size of 5, allowing the network to learn optimal weights for combining features across frames. The convolutional filter are defined as:

$$h_t^k = \sum_{i=-W/2}^{W/2} w_i \cdot x_{t+i}^k \quad (\text{B.14})$$

where  $x_t$  is the input feature,  $W$  is the kernel size, and  $w_k$  are the learnable weights.

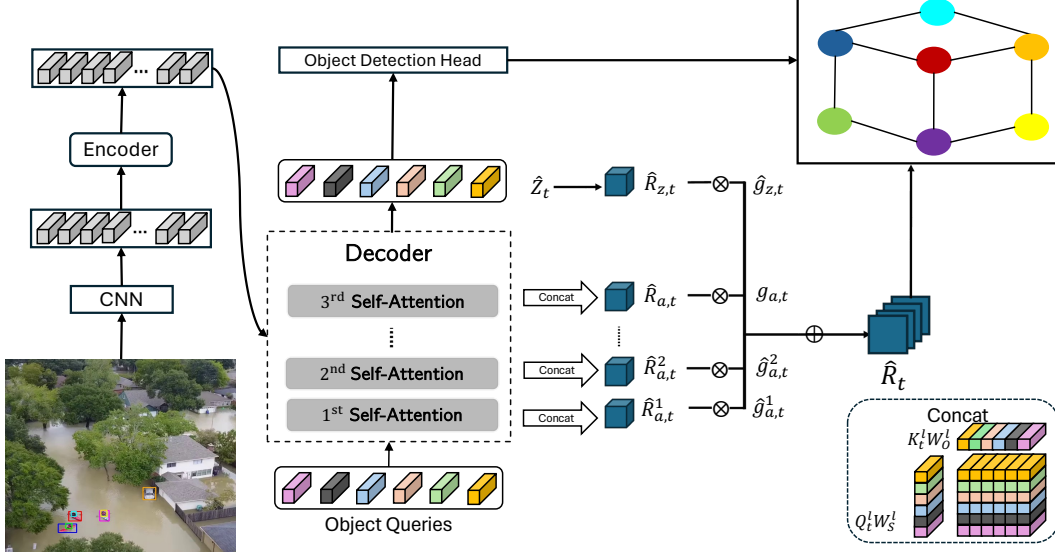


Figure B.12: Illustration of the Attention Spatial Graph, where a static graph is extracted from each frame of an input video. The nodes in the graph represent spatial regions, and the edges represent the attention-based relationships between these regions.

## B.4 Properties of the CYCLO method

### B.4.1 Spatial Attention Graph

The CYCLO model computes spatial relationships through Eqn. (1) and (2) at each layer  $l$  and for each frame  $t$ , as illustrated in Fig.B.12. This computation analyzes interactions between query and key vectors through an attention mechanism, allowing CYCLO to explicitly capture and dynamically update the relationships between objects across different layers.

The primary distinction between CYCLO and the previous approach (refer to Section 2.2 and Section B.2) lies in their mechanisms for establishing and refining object relationships in each frame. CYCLO computes relational representations for each object pair at every layer, providing a detailed and adaptable understanding of object interactions. CYCLO also enhances SGG through multi-head self-attention layers in transformer-based architectures, where each “head” focuses on different facets of relationships, yielding a comprehensive understanding of scene dynamics. In addition, the direct computation in CYCLO eliminates the need for a separate relational detection phase, reducing computational overhead and error propagation from sequential processing. Conversely, the Batch Progressive approach employs a unified self-attention mechanism within the Transformer Encoder (Eqn. (B.10)) to iteratively merge and refine relationship features.

### B.4.2 Circle and Periodic

**Fourier Transform.** The Fourier transform is a fundamental that enables the analysis and representation of periodic functions as a sum of sinusoidal components. Given a periodic function  $f(t)$  with period  $T$ , the Fourier series representation can be expressed as:

$$f(t) = \sum_{n=-\infty}^{\infty} c_n e^{i2\pi \frac{nt}{T}}, \quad (\text{B.15})$$

where the complex coefficients  $c_n$  are computed via the integral:

$$c_n = \frac{1}{T} \int_0^T f(t) e^{-i2\pi \frac{nt}{T}} dt. \quad (\text{B.16})$$

The Fourier series representation in Eqn.(B.15) expresses a periodic function as an infinite sum of complex exponentials, each representing a specific frequency component. The coefficients  $c_n$  in this representation, computed using the integral in Eqn.(B.16), capture the amplitude and phase of each

frequency component. This decomposition of a periodic function into its constituent frequencies explains its behavior and properties in the frequency domain.

**Cyclic Attention.** We leverage the Fourier transform for sequence analysis in cyclic attention (CA), which considers a periodic sequence  $K$  with period  $T$ . Inspired by the Fourier series representation, we can express the sequence  $K$  as:

$$K(t) = \sum_{n=-\infty}^{\infty} c_n e^{i2\pi \frac{nt}{T}}, \quad (\text{B.17})$$

where the coefficients  $c_n$  capture the frequency-domain characteristics of the sequence. The modulo operation in CA ensures proper handling of cyclic shifts, as shown in the following equation:

$$(t+i) \bmod T = \begin{cases} t+i-T & \text{if } t+i \geq T, \\ t+i & \text{if } t+i < T. \end{cases} \quad (\text{B.18})$$

By applying the modulo operation to the Fourier series representation of  $K$ , we obtain:

$$K_{(t+i), \bmod T} = \sum_{n=-\infty}^{\infty} c_n e^{i2\pi \frac{n(t+i)}{T}}. \quad (\text{B.19})$$

Then, we incorporate Eqn. (B.19) into the CA mechanism yields:

$$\text{CA}(Q_t, K_t) = \sum_{i=0}^{T-1} \sigma \left( \frac{Q_t \left( \sum_{n=-\infty}^{\infty} c_n e^{i2\pi \frac{n(t+i)}{T}} \right)^\top}{\sqrt{d_{\text{head}}}} \right) \quad (\text{B.20})$$

Eqn. (B.20) reveals the profound connection between cyclic attention and the Fourier transform. Our cyclic attention evaluates the interaction between the query  $Q_t$  and cyclically shifted versions of the key  $K_t$ , with each shift weighted by the corresponding Fourier series exponential term. The summation over  $i$  captures the cumulative influence of all cyclic shifts, providing a comprehensive assessment of the sequence's periodicity. In addition, by leveraging the inherent periodicity of sequences, cyclic attention effectively exploits the underlying structure analogous to how the Fourier series decomposes a function into its constituent frequencies. Each term in the summation of Eqn. (B.20) represents a specific phase shift in the Fourier series, establishing a direct link between the time-domain interactions in cyclic attention and the frequency-domain analysis in Fourier theory. Furthermore, this mathematical perspective illuminates the ability to capture and utilize the rich information embedded in the sequence's periodic structure of cyclic attention.

### B.4.3 Non-Permutation Equivariance

**Self-Attention and Permutation Equivariance.** Different from Eqn. (3), the computation for self-attention can be defined as:

$$\text{SA}(Q_t, K_t) = \text{softmax} \left( \frac{Q_t K_t^\top}{\sqrt{d_{\text{head}}}} \right) V_t \quad (\text{B.21})$$

When we apply a permutation matrix  $\pi$  to  $Q_t$  and  $K_t$ , we obtain the transformed matrices  $Q'_t = Q_t \pi$  and  $K'_t = K_t \pi$ . Given that the permutation matrix is orthogonal,  $\pi^\top = \pi^{-1}$ , we have:

$$\text{SA}(Q'_t, K'_t) = \text{softmax} \left( \frac{Q'_t K'^\top}{\sqrt{d_{\text{head}}}} \right) V_t \quad (\text{B.22})$$

$$= \text{softmax} \left( \frac{Q_t \pi (\pi^\top K_t^\top)}{\sqrt{d_{\text{head}}}} \right) V_t \quad (\text{B.23})$$

$$= \text{softmax} \left( \frac{Q_t K_t^\top}{\sqrt{d_{\text{head}}}} \right) V_t = \pi (\text{SA}(Q_t, K_t)) \quad (\text{B.24})$$

Eqn. (B.22) demonstrates that self-attention is permutation equivariant, as the output under permutation is simply a permuted version of the original output.



**Cyclic Attention and Non-Permutation Interaction.** We consider the permutation  $\pi$  applied to  $Q_t$  and  $K_t$  in Eqn. (3), leading to  $Q'_t = Q_t\pi$  and  $K'_t = K_t\pi$ :

$$\text{CA}(Q'_t, K'_t) = \text{softmax} \left( \frac{Q'_t [(K'_t)_{(t+i) \bmod T}]^\top}{\sqrt{d_{\text{head}}}} \right) V_t \quad (\text{B.25})$$

$$= \text{softmax} \left( \frac{Q_t \pi [(K_t \pi)_{(t+i) \bmod T}]^\top}{\sqrt{d_{\text{head}}}} \right) V_t \quad (\text{B.26})$$

In Eqn. (B.25), the key difficulty arises in expressing  $(K'_t)_{(t+i) \bmod T}$  due to the cyclic shift applied after the permutation. The indices affected by the cyclic shift might no longer align with those modified by the permutation, leading to:

$$(K_t \pi)_{(t+i) \bmod T} \neq (K_{(t+i) \bmod T} \pi) \quad (\text{B.27})$$

The discrepancy in Eqn. (B.27) underscores the difference between self-attention and cyclic attention regarding permutation equivariance. While self-attention treats elements based solely on their content, resulting in a permutation equivariant output, cyclic attention indicates a complex interaction between cyclic shifts and permutations. This interaction renders the output of cyclic attention under non-permutation, as the relative order of elements is altered in a way that is not simply a permutation of the original output. Consequently, cyclic attention is sensitive to the intrinsic order and continuity of the sequence, enabling it to capture the temporal relationships between objects. This property makes cyclic attention particularly well-suited for tasks where the sequential nature of the data is essential, as it can effectively model the underlying structure and dependencies present in the sequence.